Supplementary Information

Decoupling fast hydrogen oxidation reaction on a tandem electrocatalyst

Wei Guo[1], Guoqiang Zhao[2,3], Ziang Sun[4], Bingxing Zhang[1], Dongyue Xin[5], Mingxia Gao[1], Yongfeng Liu[1], Zhongbin Zhuang[5], Hai-Wei Liang[4], Hongge Pan[1,6], Wenping Sun[1,7,*]

[1]School of Materials Science and Engineering, Zhejiang University, Hangzhou 310058, P. R. China
[2]Engineering Research Center of Nano-Geomaterials of Ministry of Education, China University of Geosciences, Wuhan 430074, P. R. China
[3]Faculty of Materials Science and Chemistry, China University of Geosciences, Wuhan 430074, P. R. China
[4]Department of Chemistry, University of Science and Technology of China, Hefei 230026, P. R. China
[5]State Key Lab of Organic−Inorganic Composites and Beijing Advanced Innovation Center for Soft Matter Science and Engineering, Beijing University of Chemical Technology, Beijing 100029, P. R. China
[6]Institute of Science and Technology for New Energy, Xi'an Technological University, Xi'an 710021 P. R. China
[7]State Key Laboratory of Clean Energy Utilization, Zhejiang University, Hangzhou 310027, P. R. China

[*]Corresponding author. E-mail: wenpingsun@zju.edu.cn

Table of Contents

Supplementary Figures

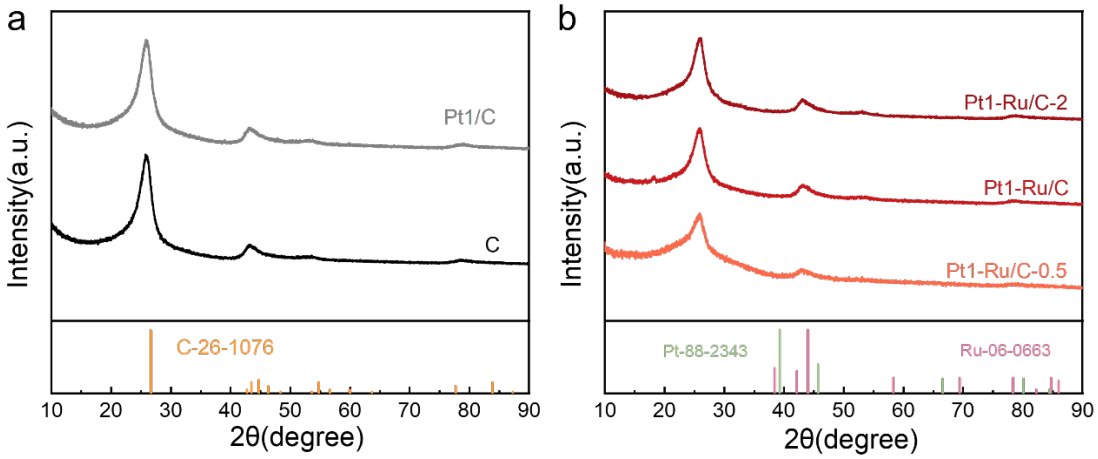

Supplementary Fig. 1: XRD patterns of a) C and Pt1/C and b) Ru/C, Pt1-Ru/C-0.5, Pt1-Ru/C, and Pt1-Ru/C-2. Source data are provided as a Source Data file.

The Pt1-Ru/C-0.5 and Pt1-Ru/C-2 catalysts were synthesized to regulate the loading of Pt single atoms (see Experimental Section for details).

Note: Pt1 represents single-atom Pt, Ru denotes Ru nanoclusters, C stands for the carbon support, and x indicates the amount of H_2PtCl_6 used during impregnation, with 60 μL as the baseline volume.

For example: Pt1-Ru/C refers to the catalyst prepared by impregnating 20 mg of Ru/C with 60 μL of 0.01 M H_2PtCl_6 solution (x=1, which is omitted for simplicity). Pt1-Ru/C-2 corresponds to the catalyst prepared by impregnating 20 mg of Ru/C with 120 μL of 0.01 M H_2PtCl_6 solution (i.e., x=2), and so on.

Additionally, Pt1-Ru/C-x-A represents the Pt1-Ru/C-x catalyst after activation under HOR overpotentials.

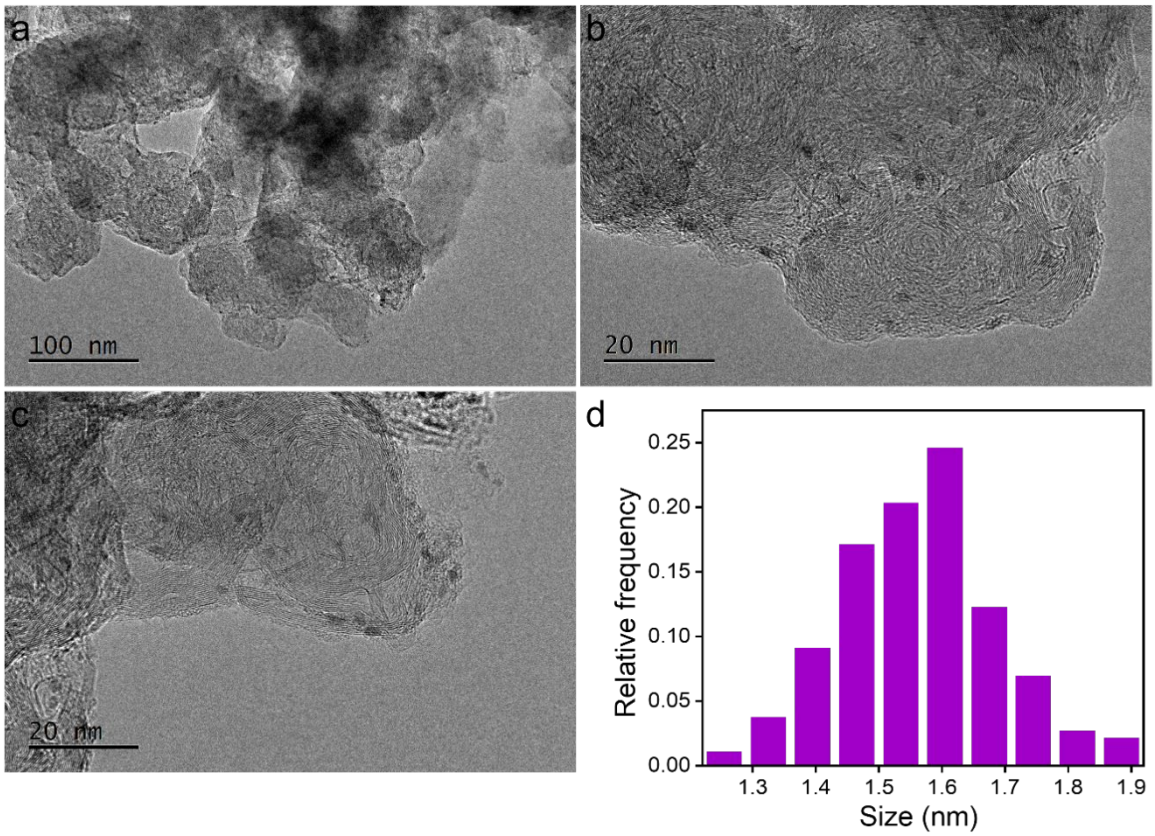

Supplementary Fig. 2: a) TEM, b,c) HR-TEM, and d) nanocluster size distribution diagrams of Ru/C.

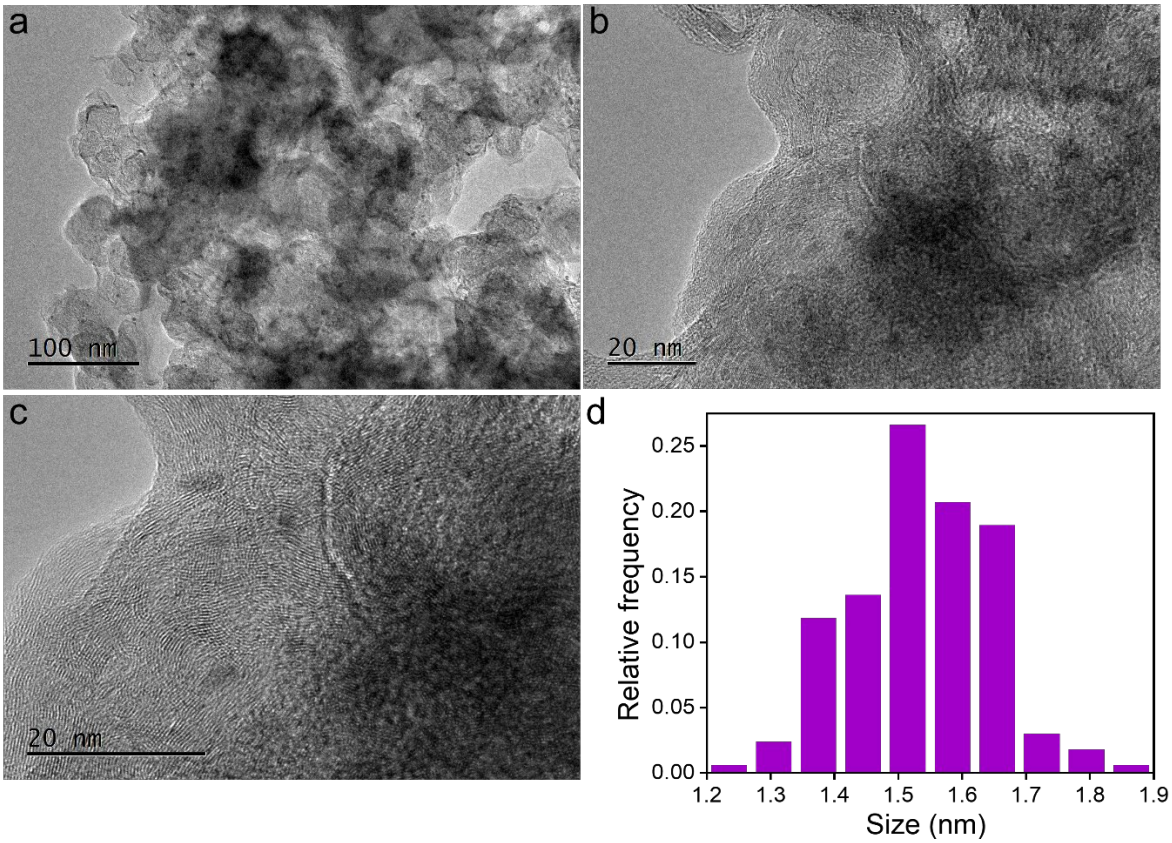

Supplementary Fig. 3: a) TEM, b,c) HR-TEM, and d) nanocluster size distribution diagrams of Pt1-Ru/C-0.5.

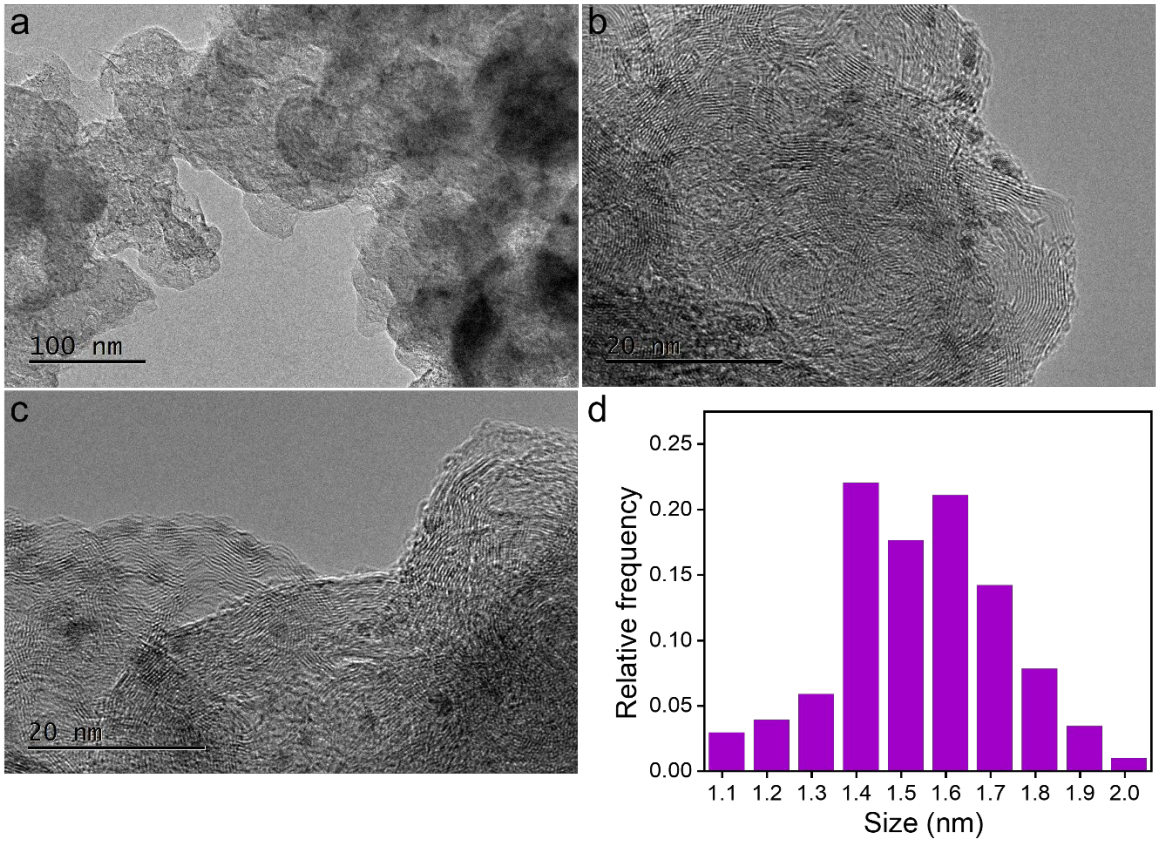

Supplementary Fig. 4: a) TEM, b,c) HR-TEM, and d) nanocluster size distribution diagrams of Pt1-Ru/C.

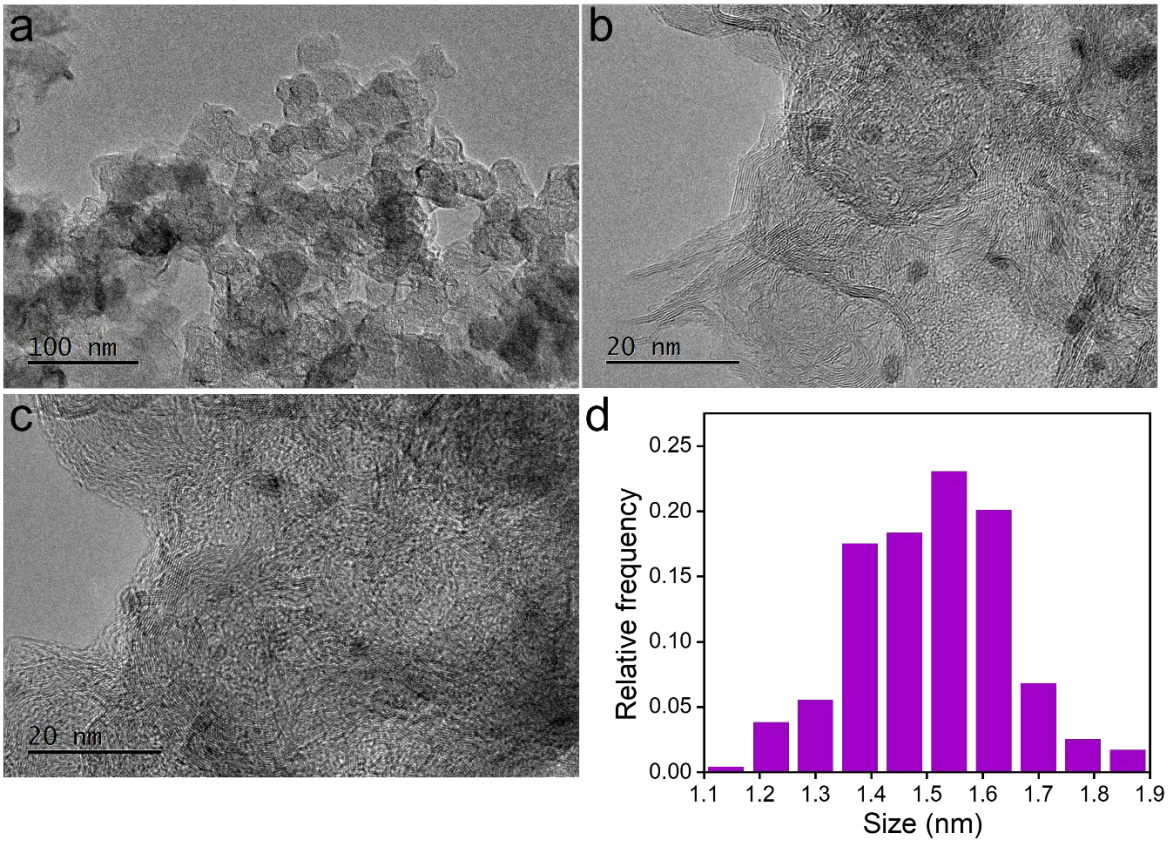

Supplementary Fig. 5: a) TEM, b,c) HR-TEM, and d) nanocluster size distribution diagrams of Pt1-Ru/C-2.

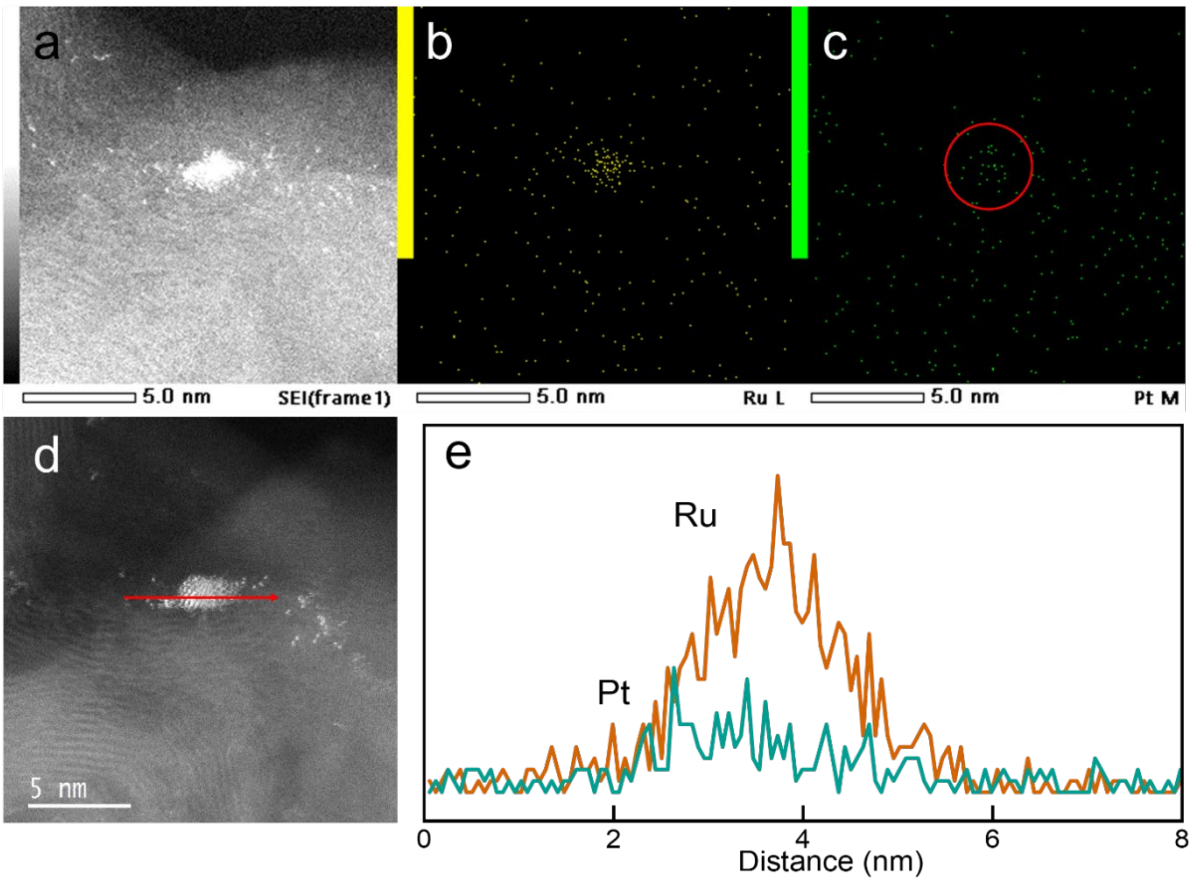

Supplementary Fig. 6: a) The STEM image and b-c) the EDS elemental mapping of Pt1-Ru/C. d-e) HAADF-STEM and EDS line-scanning profile of Pt1-Ru/C. Source data are provided as a Source Data file.

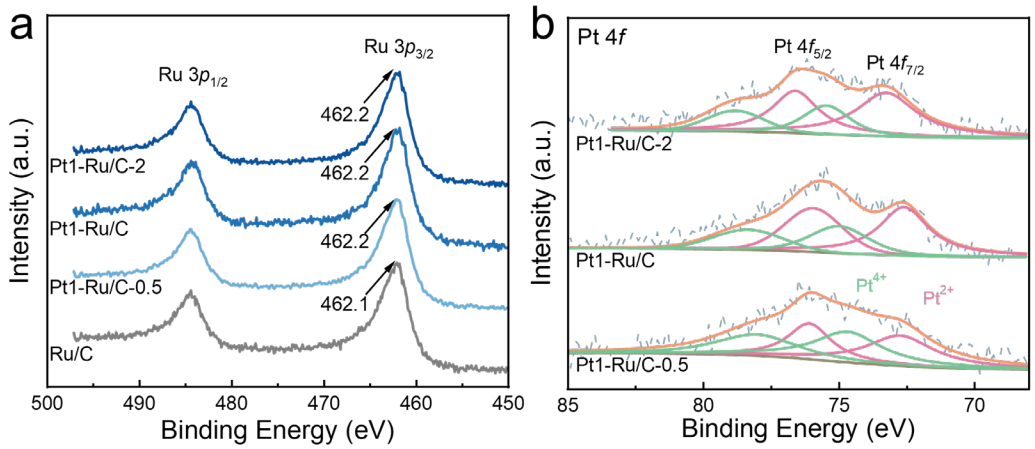

Supplementary Fig. 7: a) Ru 3*p* X-ray photoelectron spectroscopy (XPS) spectra of Ru/C, Pt1-Ru/C-0.5, Pt1-Ru/C, and Pt1-Ru/C-2. b) Pt 4*f* XPS spectra of Pt1-Ru/C-0.5, Pt1-Ru/C, and Pt1-Ru/C-2. Source data are provided as a Source Data file.

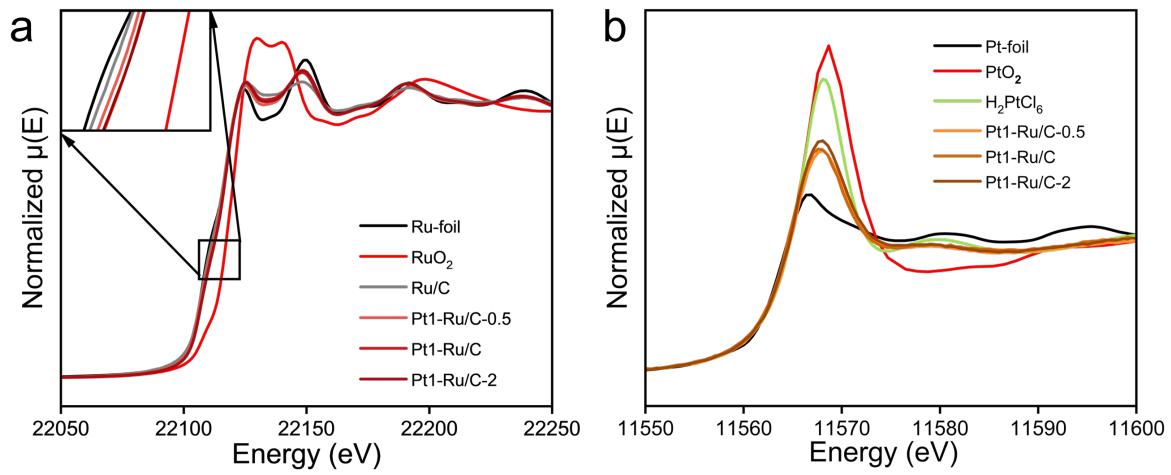

Supplementary Fig. 8: a) Ru K-edge XANES spectra of Ru-foil, RuO_2, Ru/C, Pt1-Ru/C-0.5, Pt1-Ru/C, and Pt1-Ru/C-2. b) Pt L_3-edge XANES spectra of Pt-foil, PtO_2, H_2PtCl_6, Ru/C, Pt1-Ru/C-0.5, Pt1-Ru/C, and Pt1-Ru/C-2. Source data are provided as a Source Data file.

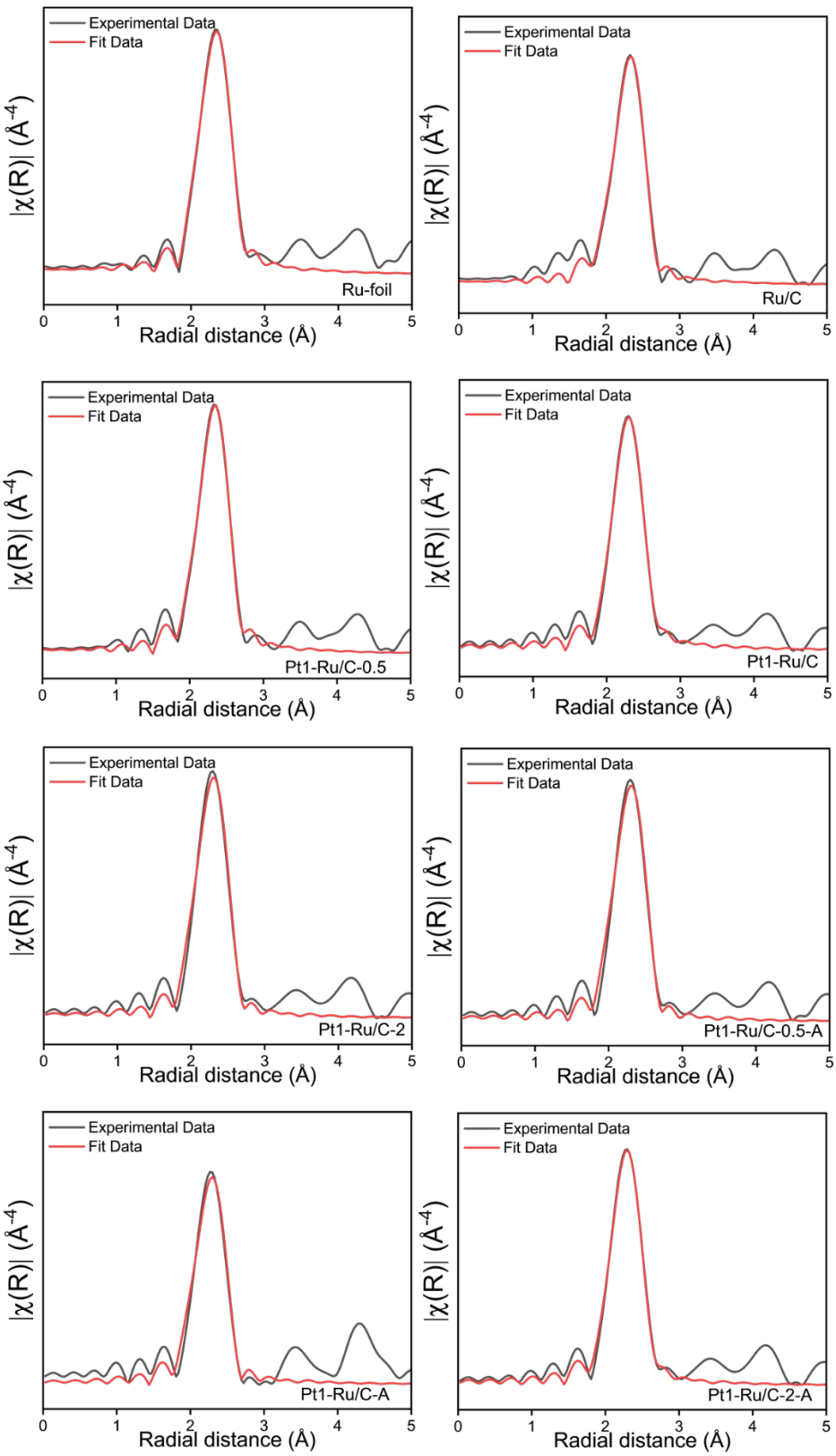

Supplementary Fig. 9: The Ru K-edge fitted EXAFS spectra of Ru foil, Ru/C, Pt1-Ru/C-0.5, Pt1-Ru/C, Pt1-Ru/C-2, Pt1-Ru/C-0.5-A, Pt1-Ru/C-A, and Pt1-Ru/C-2-A. Source data are provided as a Source Data file.

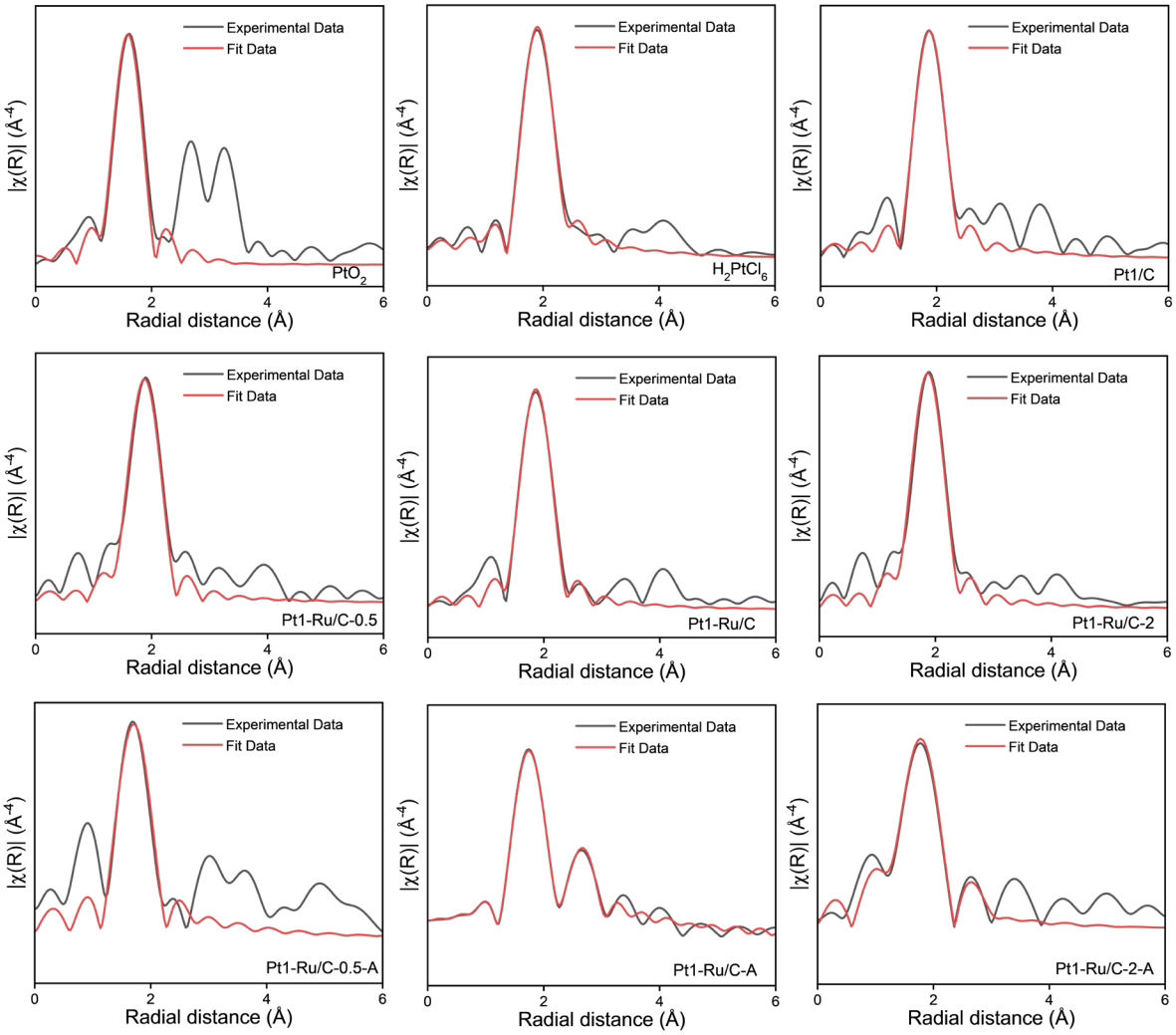

Supplementary Fig. 10: The Pt L_3-edge fitted EXAFS spectra of PtO_2, H_2PtCl_6, Pt1/C, Pt1-Ru/C-0.5, Pt1-Ru/C, Pt1-Ru/C-2, Pt1-Ru/C-0.5-A, Pt1-Ru/C-A, and Pt1-Ru/C-2-A. Source data are provided as a Source Data file.

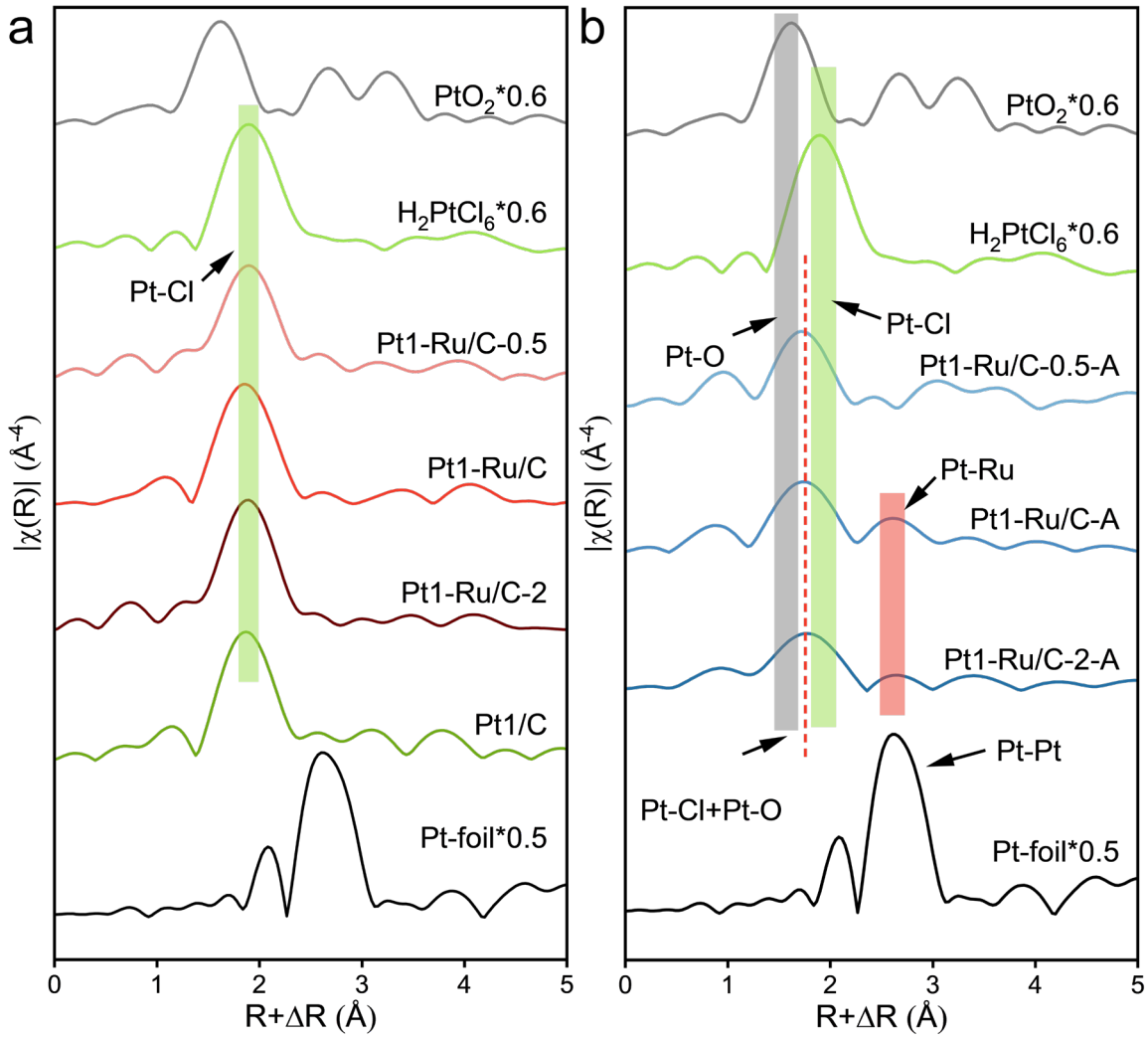

Supplementary Fig. 11: a) the Pt L_3-edge EXAFS spectra of Pt-foil, PtO_2, H_2PtCl_6, Pt1/C, Pt1-Ru/C-0.5, Pt1-Ru/C, and Pt1-Ru/C-2. b) the Pt L_3-edge EXAFS spectra of Pt-foil, PtO_2, H_2PtCl_6, Pt1-Ru/C-0.5-A, Pt1-Ru/C-A, and Pt1-Ru/C-2-A. Source data are provided as a Source Data file.

The absence of Pt-Ru bonds in the Pt1-Ru/C-0.5-A sample is likely attributed to its ultralow Pt content, which generates a weak EXAFS signal, causing the longer-range metal-metal coordination features to be obscured by noise. In contrast, the lower Pt-Ru coordination number (Supplementary Table 3) observed in the Pt1-Ru/C-2-A sample (compared with Pt1-Ru/C-A) presumably arises that a higher proportion of Pt single atoms are anchored on the carbon support rather than interacting with Ru nanoclusters, resulting in a reduced average coordination number for Pt-Ru bonds.

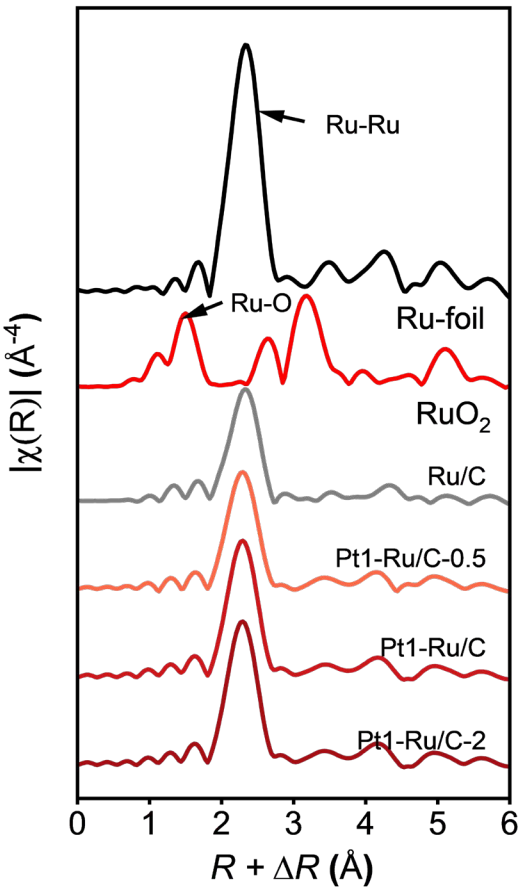

Supplementary Fig. 12: The Ru K-edge EXAFS spectra of RuO_2, Ru-foil, Ru/C, Pt1-Ru/C-0.5, Pt1-Ru/C, and Pt1-Ru/C-2. Source data are provided as a Source Data file.

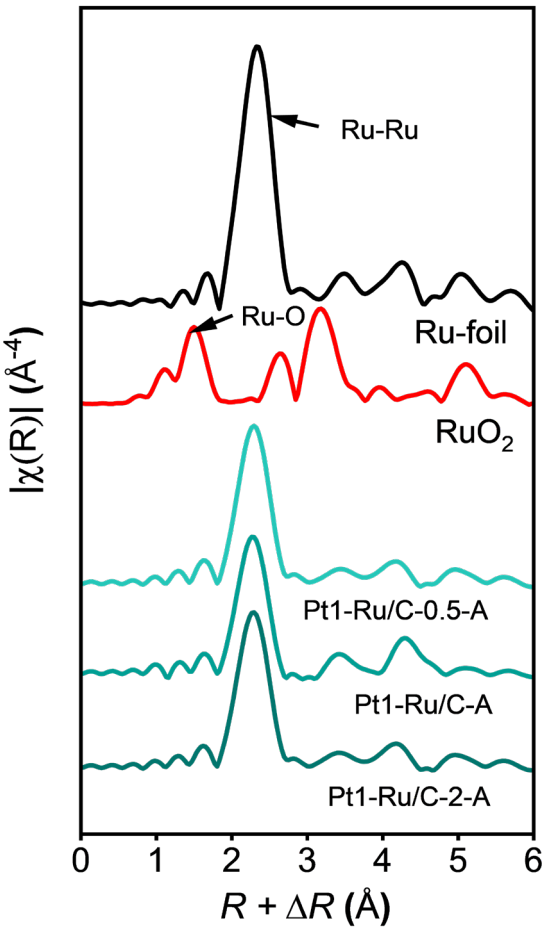

Supplementary Fig. 13: The Ru K-edge EXAFS spectra of RuO_2, Ru-foil, Pt1-Ru/C-0.5-A, Pt1-Ru/C-A, and Pt1-Ru/C-2-A. Source data are provided as a Source Data file.

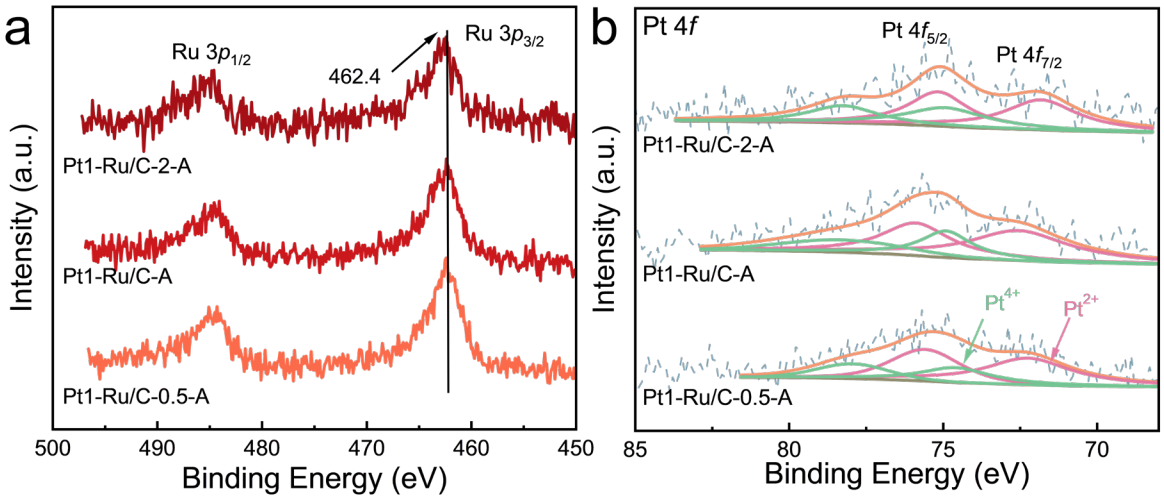

Supplementary Fig. 14: a) The Ru 3*p* and b) the Pt 4*f* XPS spectra of Pt1-Ru/C-0.5-A, Pt1-Ru/C-A, and Pt1-Ru/C-2-A. Source data are provided as a Source Data file.

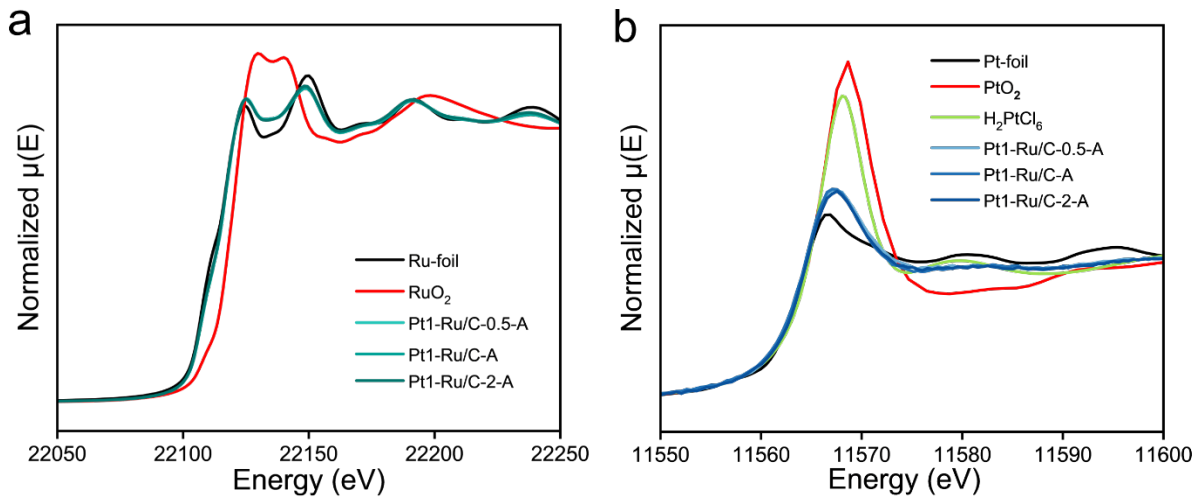

Supplementary Fig. 15: a) the Ru K-edge XANES spectra of Ru-foil, RuO_2, Pt1-Ru/C-0.5-A, Pt1-Ru/C-A, and Pt1-Ru/C-2-A. b) the Pt L_3-edge XANES spectra of Pt-foil, PtO_2, H_2PtCl_6, Pt1-Ru/C-0.5-A, Pt1-Ru/C-A, and Pt1-Ru/C-2-A. Source data are provided as a Source Data file.

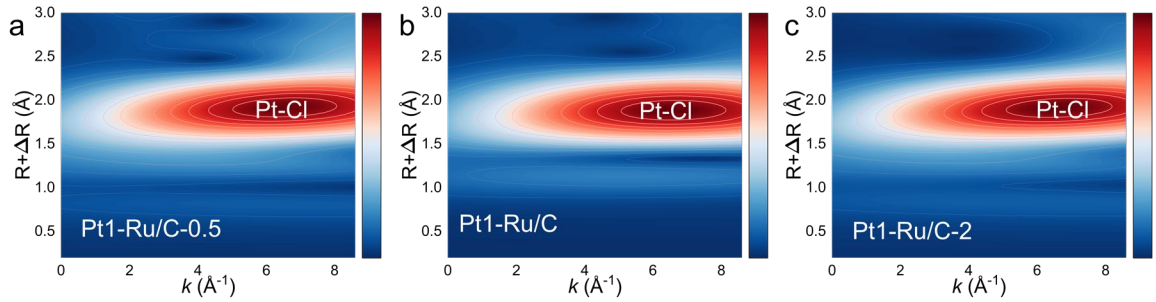

Supplementary Fig. 16: The continuous Cauchy wavelet transform (CCWT) for the k^3-weighted EXAFS signals at the a) Pt1-Ru/C-0.5, b) Pt1-Ru/C, and c) Pt1-Ru/C-2. Source data are provided as a Source Data file.

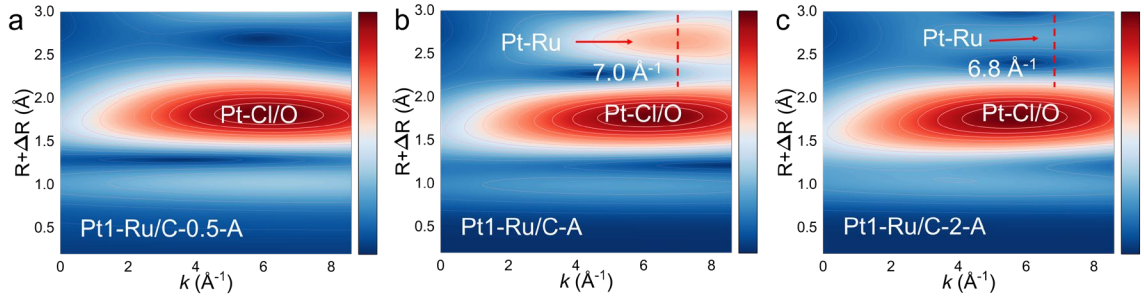

Supplementary Fig. 17: The continuous Cauchy wavelet transform (CCWT) for the k^3-weighted EXAFS signals at the a) Pt1-Ru/C-0.5-A, b) Pt1-Ru/C-A, and c) Pt1-Ru/C-2-A. Source data are provided as a Source Data file.

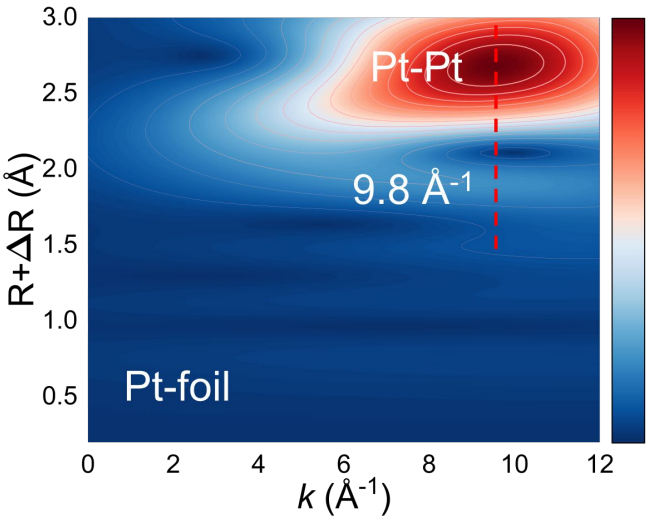

Supplementary Fig. 18: The continuous Cauchy wavelet transform (CCWT) for the k^3-weighted EXAFS signals at the Pt-foil. Source data are provided as a Source Data file.

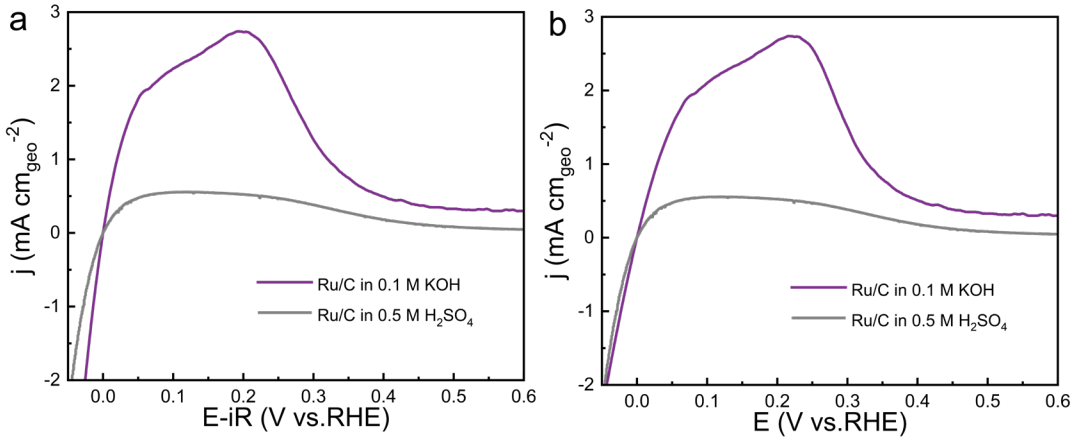

Supplementary Fig. 19: a) Geometric area-normalized LSV curves of Ru/C in different solution. All LSV data were carried out at a scan rate of 0.5 mV s^{-1} with 90% iR compensation on a RDE at 1600 rpm. The ohmic resistance (50± 5 Ω and 5 ± 0.3 Ω in 0.1 M KOH and 0.5 M H_2SO_4, respectively) for iR compensation was obtained from EIS analysis with a geometric area of 0.19625 cm^2. b) Geometric area-normalized LSV curves of Ru/C in different solution without iR correction. Source data are provided as a Source Data file.

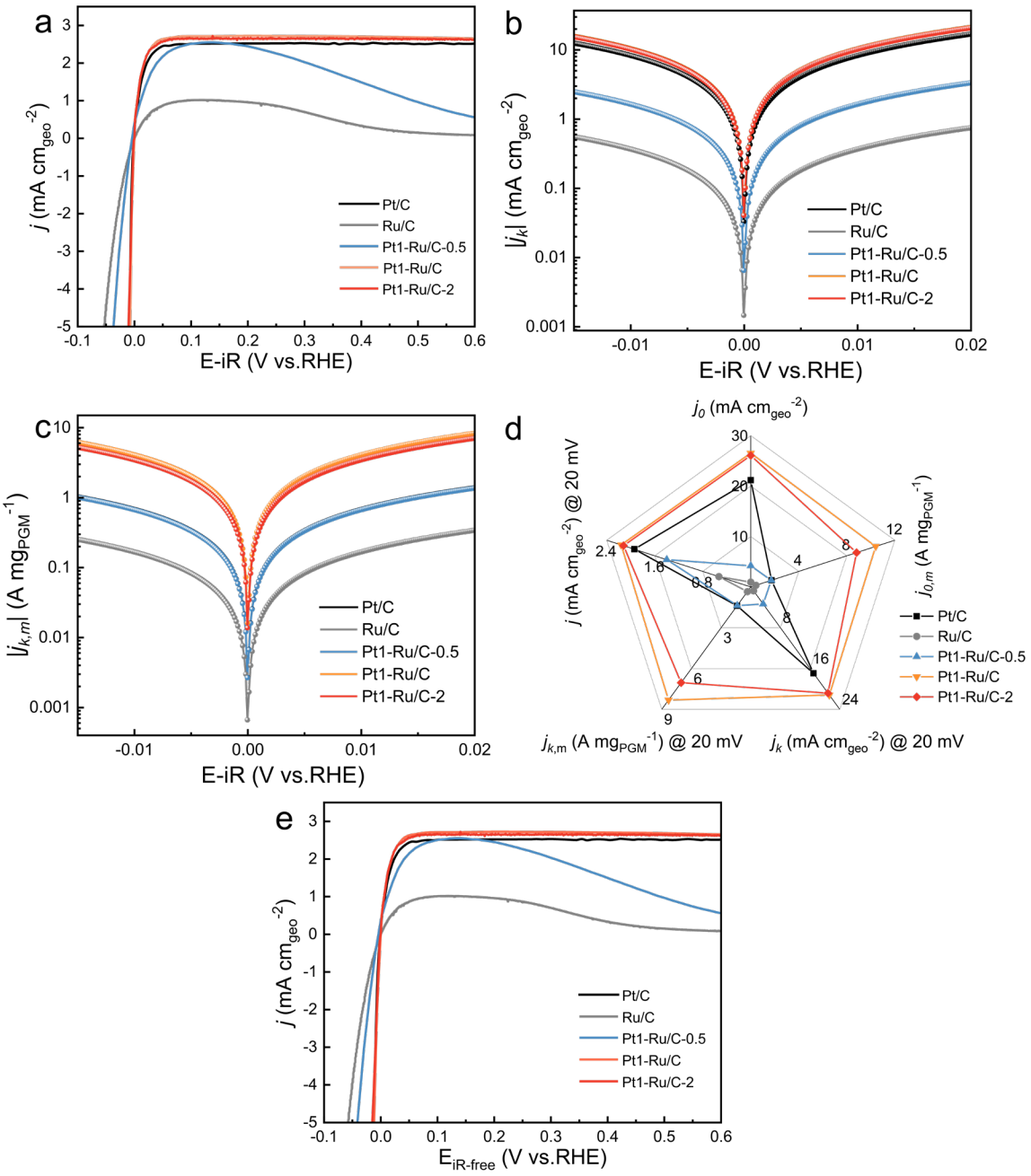

Supplementary Fig. 20: Electrochemical measurement results. a) Geometric area-normalized LSV curves of different catalysts. b) Calculated HOR kinetic current densities (j_k) versus potential plots recorded from (a). c) PGM mass-normalized HOR kinetic current densities (j_k) versus potential plots. d) Comparison of j_k, $j_{k,m}$ (mass-normalized j_k), and j at an overpotential of 20 mV and j_0, $j_{0,m}$ (mass-normalized j_0) of different catalysts. All LSV data were carried out at a scan rate of 0.5 mV s^{-1} with 90% iR compensation on a RDE at 1600 rpm. The ohmic resistance ($5 \pm 0.3\ \Omega$) for iR compensation was obtained from EIS analysis

with a geometric area of 0.19625 cm². e) Geometric area-normalized LSV curves of different catalysts without iR correction. Source data are provided as a Source Data file.

As manifested in Supplementary Fig. 20d, the Pt1-Ru/C catalyst possesses the mass-normalized exchange current density $j_{0,m}$ of 10.41 A mg_{PGM}^{-1}, which is higher than those of Pt/C (1.73 A mg_{PGM}^{-1}), Ru/C (0.43 A mg_{PGM}^{-1}). At an overpotential of 20 mV, the Pt1-Ru/C catalyst demonstrates an impressive mass-normalized kinetic current density ($j_{k,m}$) of 8.3 A mg_{PGM}^{-1}, surpassing Pt/C by fivefold, where they achieved only 1.4 mg_{PGM}^{-1} (Supplementary Fig. 20c-d).

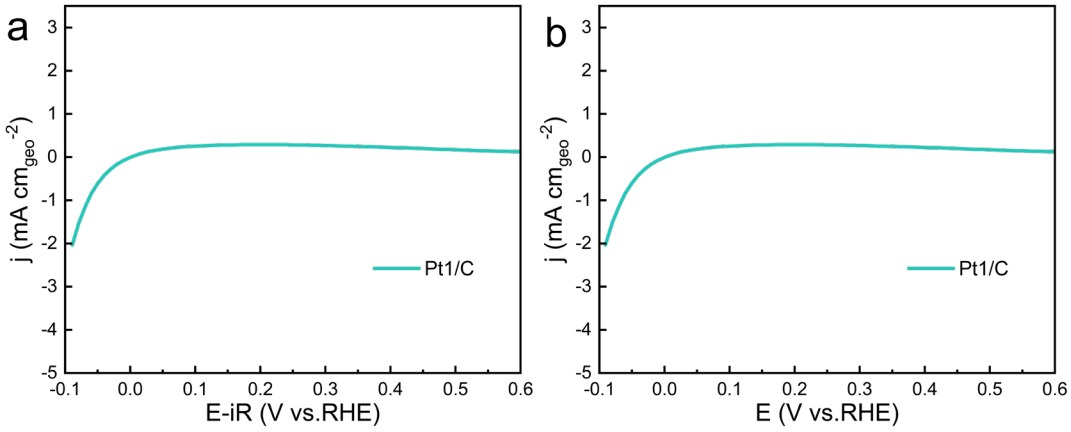

Supplementary Fig. 21: a) Geometric area-normalized LSV curves of Pt1/C. The LSV data were carried out at a scan rate of 0.5 mV s^{-1} with 90% iR compensation on a RDE at 1600 rpm. The ohmic resistance ($5 \pm 0.3\ \Omega$) for iR compensation was obtained from EIS analysis with a geometric area of 0.19625 cm^2. b) Geometric area-normalized LSV curves of Pt1/C without iR correction. Source data are provided as a Source Data file.

To eliminate the influence of Pt single atoms on the carbon support in the catalytic reaction, chloroplatinic acid is directly impregnated on the carbon support to prepare Pt1/C (see Experimental Section for details). The structural characterization of Pt1/C is shown in Supplementary Fig. 11 and Supplementary Fig. 22.

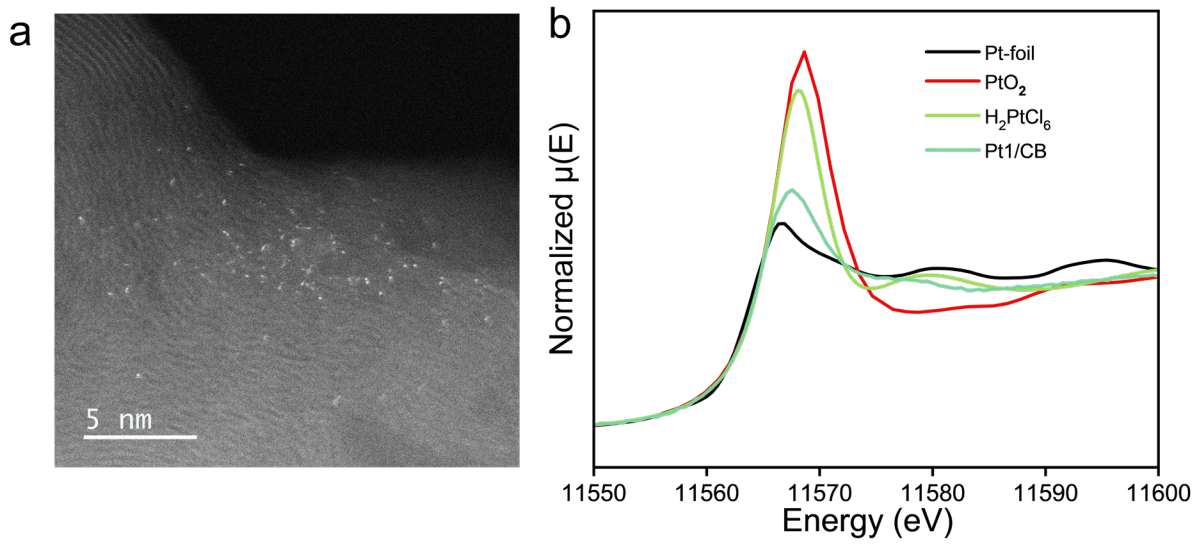

Supplementary Fig. 22: a) The HAADF-STEM image and of Pt1/C. b) The Pt L_3-edge XANES spectra of Pt-foil, PtO_2, H_2PtCl_6, and Pt1/C. Source data are provided as a Source Data file.

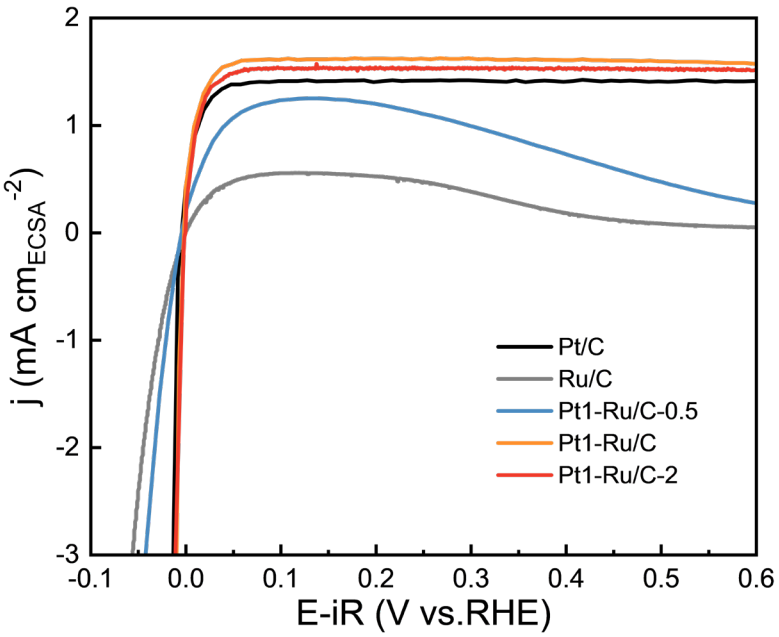

Supplementary Fig. 23: The ECSA-normalized LSV curves of different catalysts. Source data are provided as a Source Data file.

The ECSAs were determined by copper underpotential deposition (Cu-UPD) cyclic voltammetry (Supplementary Fig. 24).

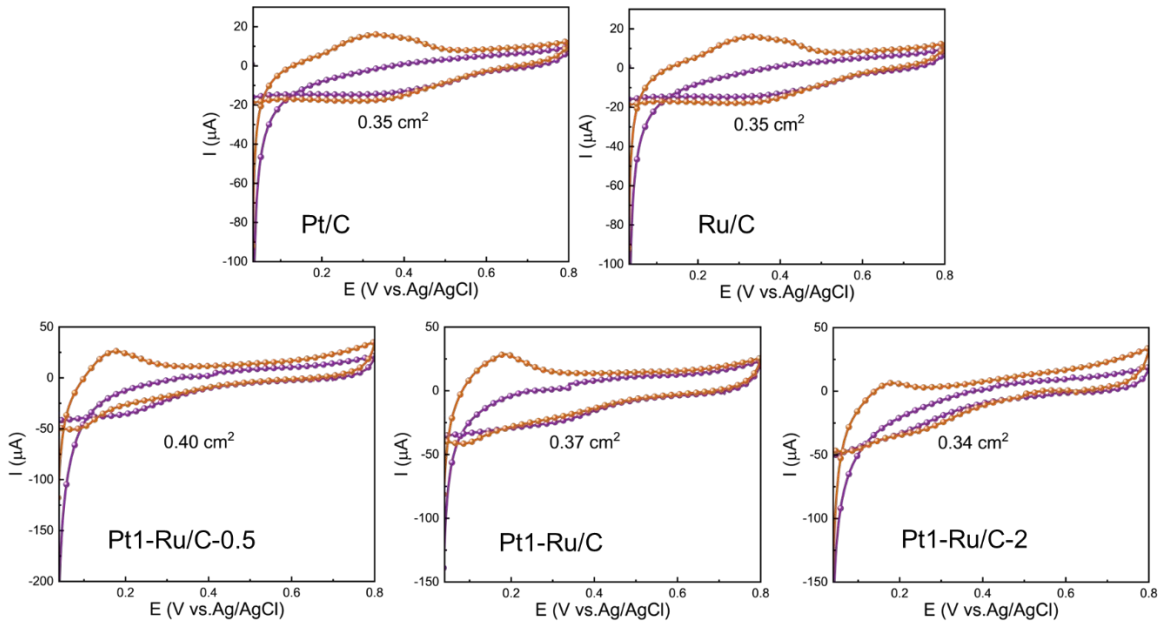

Supplementary Fig. 24: Estimation of the ECSA using the copper underpotential deposition (Cu-UPD) method for Pt/C, Ru/C, Pt1-Ru/C-0.5, Pt1-Ru/C, and Pt1-Ru/C-2. These CV data are iR correction free. Source data are provided as a Source Data file.

Note: The preparation process of the working electrode involves dropping different volumes of catalyst ink onto a glassy carbon electrode, where the catalyst concentration for Pt/C working electrodes is 12 $\mu g_{PGM}/cm^2$, and for Ru/C and Ru/C-Ptx working electrodes is 2 $\mu g_{PGM}/cm^2$. The effective area of the working electrode is 0.19625 cm^2.

Voltammogram curves were acquired in 0.5 M H_2SO_4 solutions in the absence (purple) and presence (orange) of 5 mM $CuCl_2$. Three tests were performed to evaluate the ECSA for each catalyst.

For Cu-UPD test, to obtain monolayered Cu deposited on metal, the Pt/C, Pt/Ru/C, and Ru-based electrodes were polarized at underpotentially deposited potentials for 100s in an Ar-purged 0.5 M H_2SO_4 solution containing 5 mM of $CuCl_2$. Then, the Cu-UPD stripping voltammetry was performed by oxidizing the deposited Cu between the underpotentially deposited potential and 0.7 V at a scan rate of 10 mV s^{-1} (red curves). The voltammogram curve (black curve) of each catalyst in 0.5 M H_2SO_4 solution without $CuCl_2$ was applied as the background for the corresponding Cu-UPD stripping voltammogram. The ECSA was

evaluated from the integral area of Cu-UPD peaks (Q_{Cu}) with the subtraction of the background and a charge density of 420 μC cm^{-2} (Q_s):

$$\text{ECSA}\left(\frac{m^2_{metal}}{g_{metal}}\right)=\frac{Q_{Cu}}{M_{metal}\,Q_s}$$

where M_{metal} is the metal mass loading on a certain geometric area of the working electrode.

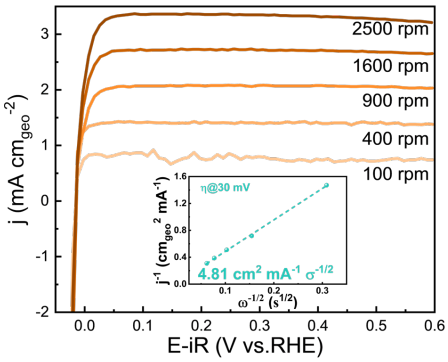

Supplementary Fig. 25: LSV curves of Pt1-Ru/C at various rotation rates, and the inset shows the Koutecky–Levich plot at an overpotential of 30 mV. All LSV data were carried out at a scan rate of 0.5 mV s^{-1} with 90% iR compensation on a RDE at 1600 rpm. The ohmic resistance ($5 \pm 0.3\ \Omega$) for iR compensation was obtained from EIS analysis with a geometric area of 0.19625 cm^2. Source data are provided as a Source Data file.

The polarization curves collected at different rotation speeds for the Pt1-Ru/C catalyst are shown in Supplementary Fig. 25. As the rotation speed increases, the limit current density correspondingly increases due to improved mass transport.[1,2] A linear relationship between $\omega^{-1/2}$ and the inverse of current density at an overpotential of 30 mV is observed in the Koutecky–Levich plots. The slopes are calculated to be 4.81 cm^2 mA^{-1} $s^{-1/2}$ for Pt1-Ru/C, which is close to the theoretical value for a two-electron reaction of 4.87 cm^2 mA^{-1} $s^{-1/2}$.[2,3]

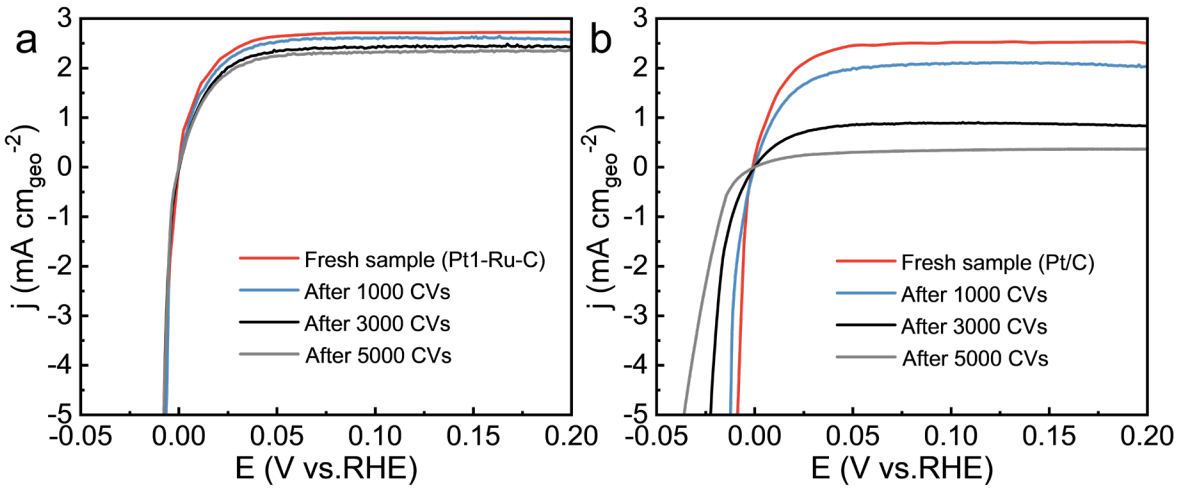

Supplementary Fig. 26: ADT results of a) Pt1-Ru/C and b) Ru/C in H_2-saturated 0.5 M H_2SO_4. The durability tests were performed by running repetitive CV scans from −0.05 to 0.1 V (vs. RHE) at a sweep rate of 150 mV s^{-1}. The LSV curves were recorded after 0, 1000, 3000, and 5000 CV scans, respectively. All LSV data were carried out at a scan rate of 0.5 mV s^{-1} with 90% iR compensation on a RDE at 1600 rpm. The ohmic resistance ($5 \pm 0.3\ \Omega$) for iR compensation was obtained from EIS analysis with a geometric area of 0.19625 cm^2. Source data are provided as a Source Data file.

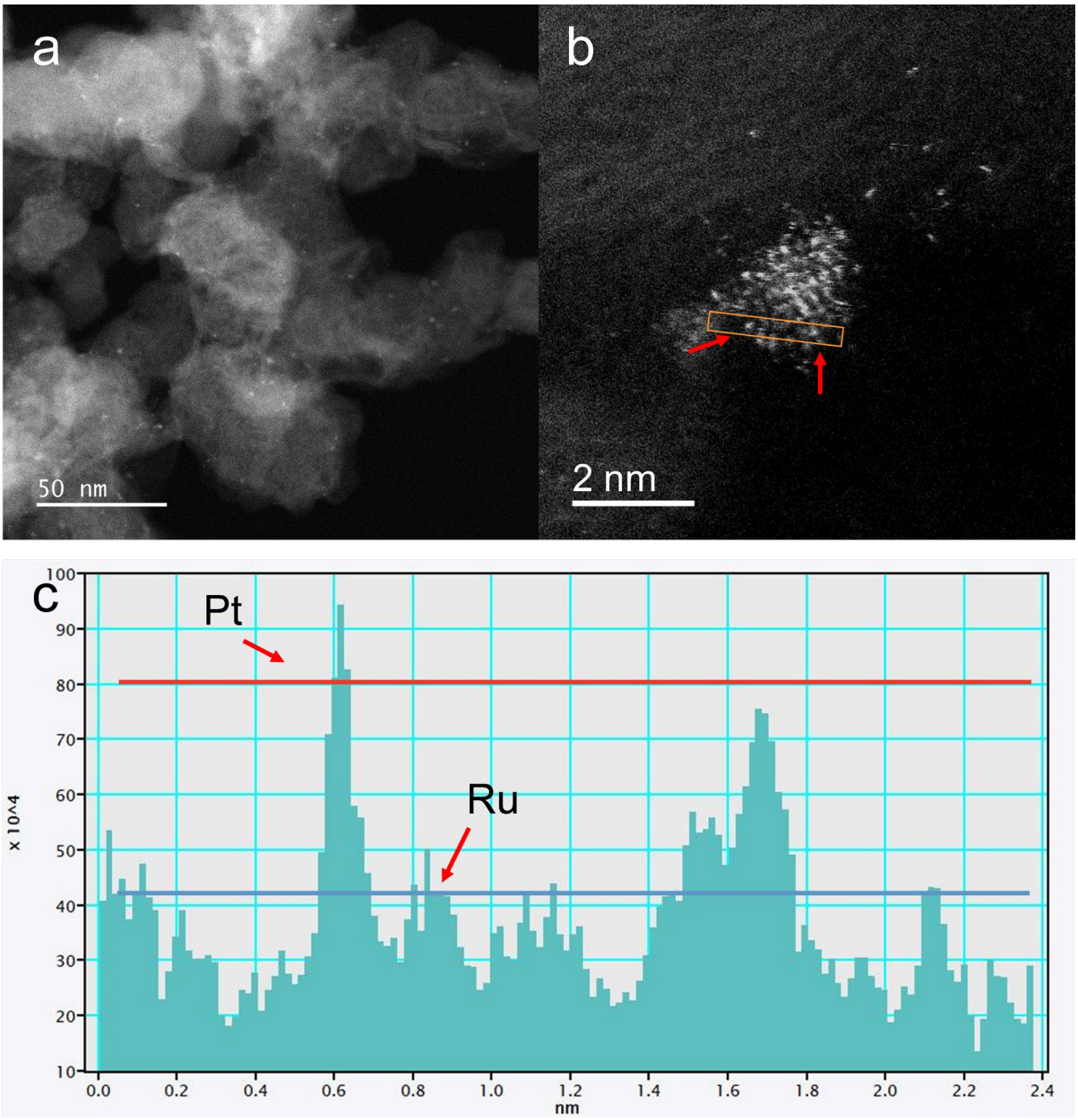

Supplementary Fig. 27: a) TEM, b) HAADF-STEM images and c) the intensity profiles (corresponding to the yellow boxed regions in Supplementary Fig. 27b) of Pt1-Ru/C after the accelerated durability test in the 0.5 M H_2SO_4. Source data are provided as a Source Data file.

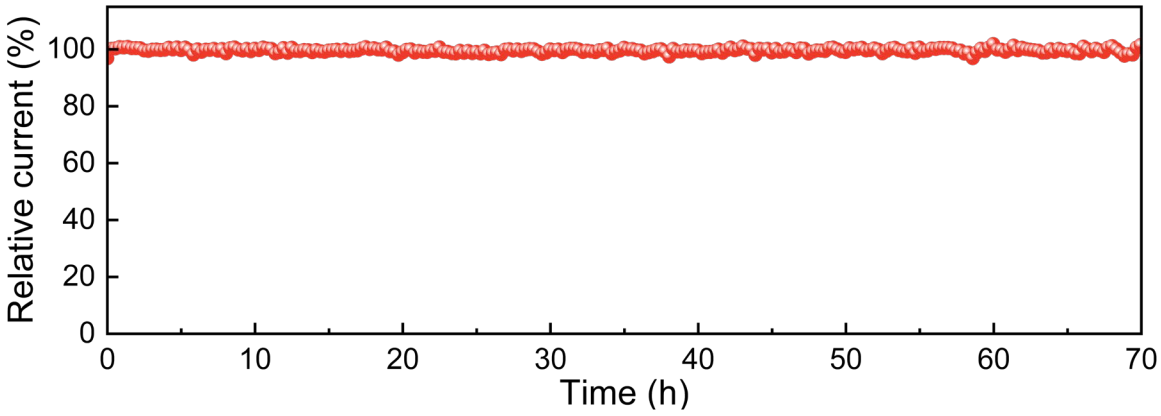

Supplementary Fig. 28: HOR stability test. Relative current-time chronoamperometry response of Pt1-Ru/C in a H_2-saturated aqueous solution of 0.5 M H_2SO_4 at an overpotential of 20 mV. Source data are provided as a Source Data file.

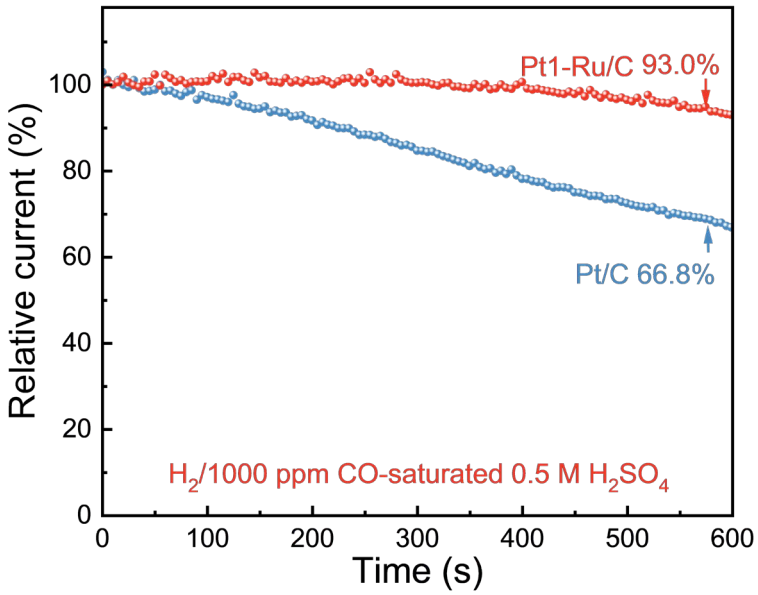

Supplementary Fig. 29: Relative chronoamperometry response of Pt1-Ru/C and Pt/C in H_2/1000 ppm CO-saturated 0.5 M H_2SO_4 solution at 0.1 V (vs. RHE). Source data are provided as a Source Data file.

The current density of Pt1-Ru/C decreases by 7% after continuous operation for 600 s, while the Pt/C catalyst diminishes by 33.2%.

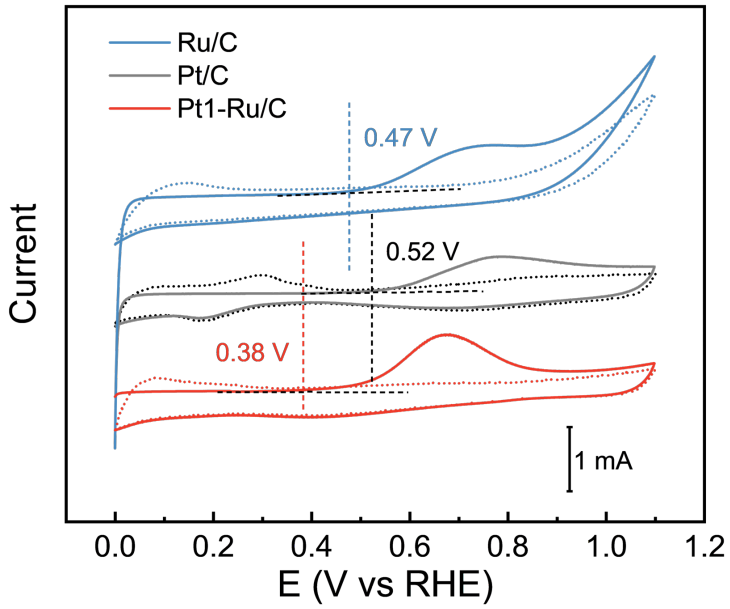

Supplementary Fig. 30: The CO-stripping measurements for Pt1-Ru/C, Ru/C, and Pt/C. CO adsorption was firstly performed with amperometric i-t test at 0.05 V vs. RHE for 10 min in a CO-saturated 0.1 M KOH solution. Then the electrode was transferred into a N_2-saturated 0.1 M KOH solution. The CO stripping current was obtained by CV in the potential range of 0-1.1 V vs. RHE at a scan rate of 50 mV s^{-1}. These CV data are iR correction free. Source data are provided as a Source Data file.

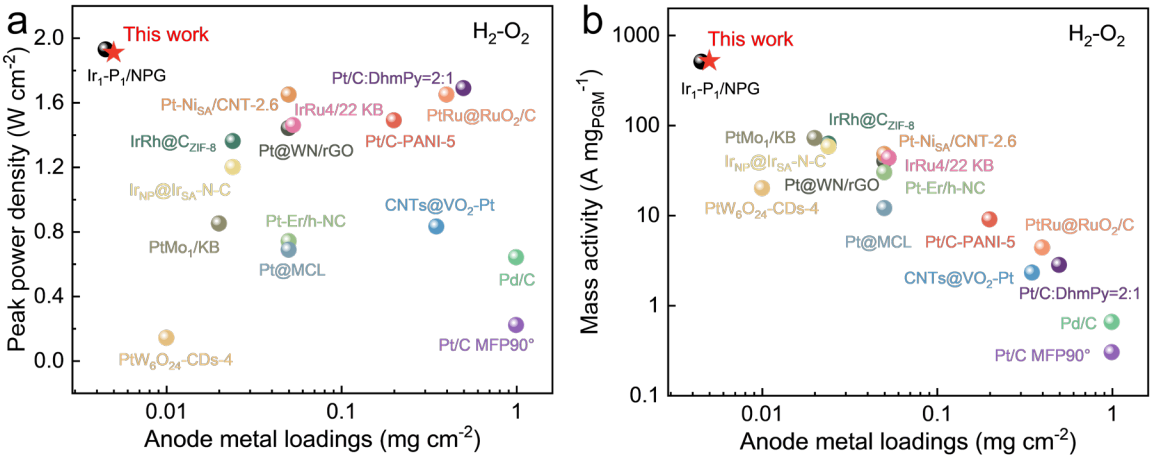

Supplementary Fig. 31: The comparisons of a) the peak power densities and b) the mass activity at 0.6 V normalized by the mass of anode metal of PEMFCs for H_2-O_2 as feeding gas (detail shown in Supplementary Table S5).

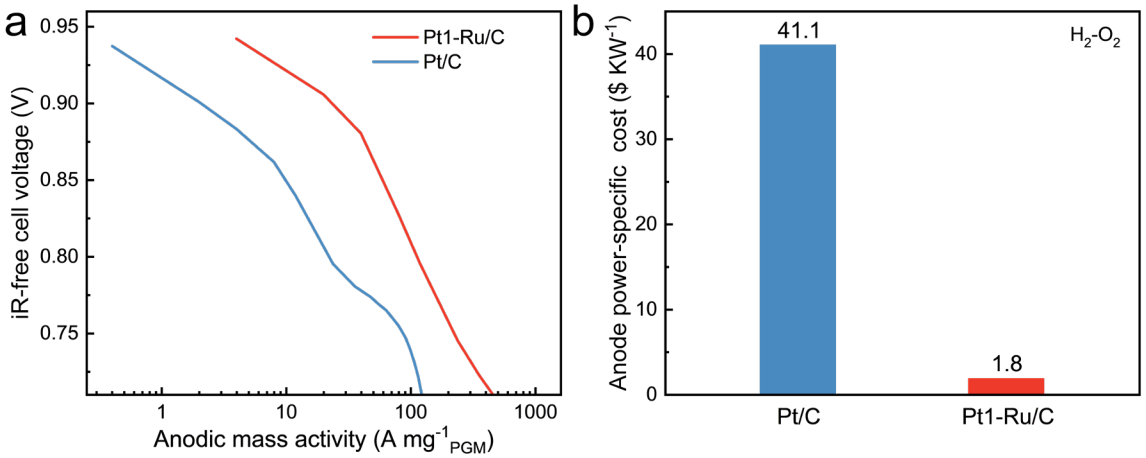

Supplementary Fig. 32: a) Anodic mass activity Tafel plots derived from MEA measurements. b) H_2–O_2 fuel cell anode power-specific cost. The PEMFC polarization curves are not iR corrected. Source data are provided as a Source Data file.

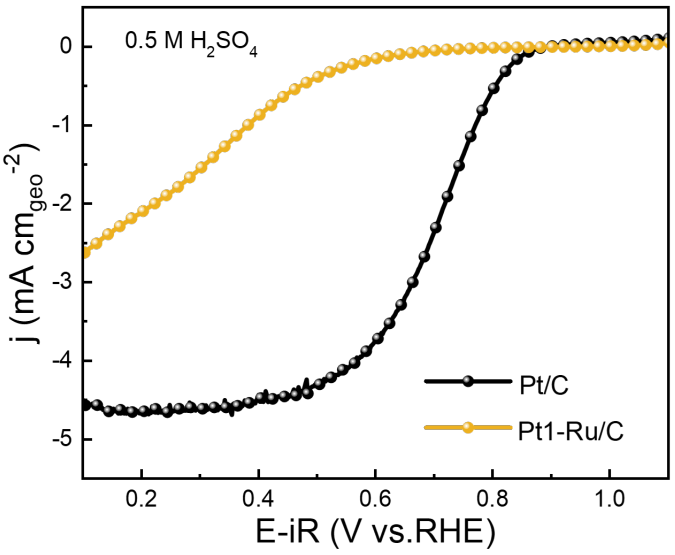

Supplementary Fig. 33: Geometric area-normalized LSV curves of Pt/C and Pt1-Ru/C. All LSV data were carried out at a scan rate of 0.5 mV s^{-1} with 90% iR compensation on a RDE at 1600 rpm. The ohmic resistance ($5 \pm 0.3\ \Omega$) for iR compensation was obtained from EIS analysis with a geometric area of 0.19625 cm^2. Source data are provided as a Source Data file.

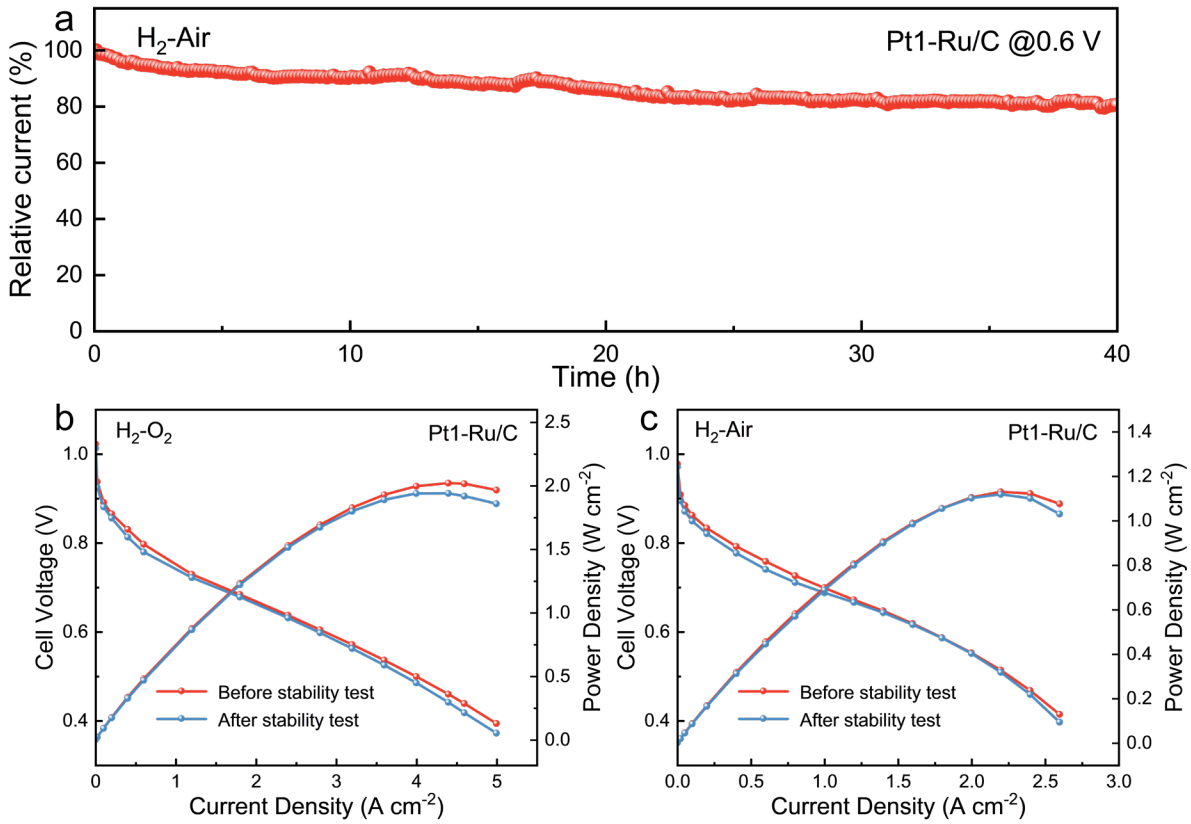

Supplementary Fig. 34: a) Long-term stability tests of the H_2-Air fuel cell at 0.6 V using the Pt1-Ru/C (0.005 mg_{PGM} cm^{-2}) as the anode catalyst. Polarization and power density plots of the PEMFC made with the anode catalyst of Pt1-Ru/C before and after the long-term stability test at 0.6 V for 40 h under H_2-air condition. b) H_2-O_2 and c) H_2-air. Test conditions: cell temperature at 80 °C, H_2 flow rate at 1 L min^{-1} and O_2/Air flow rate at 2 L min^{-1}, symmetric back pressures at 250 Kpa. The PEMFC polarization curves are not iR corrected. Source data are provided as a Source Data file.

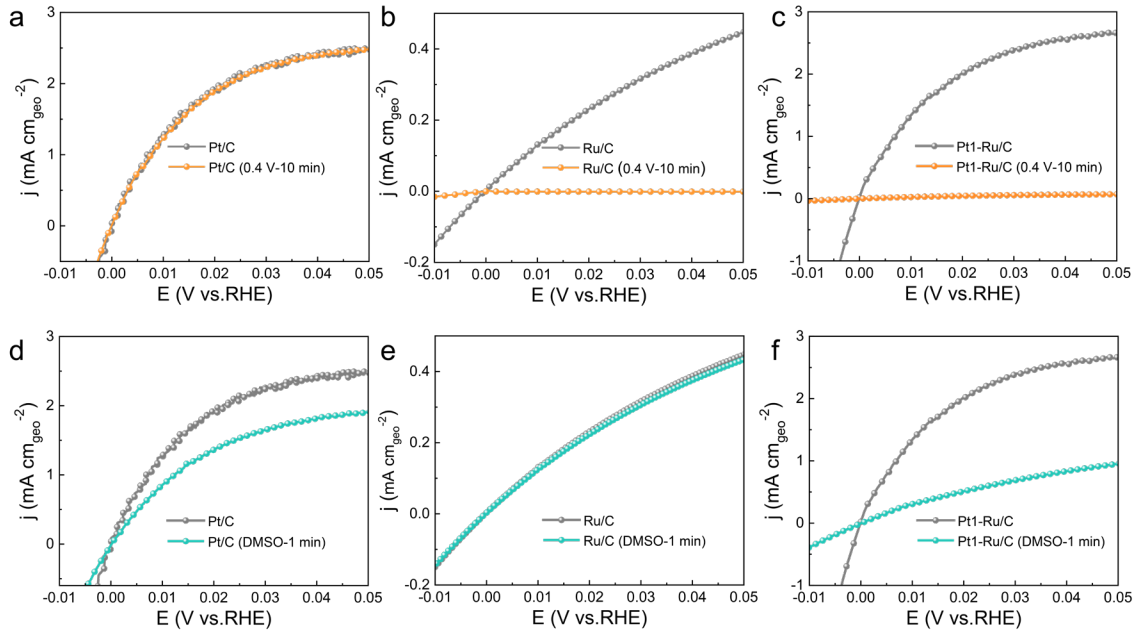

Supplementary Fig. 35: Electrochemical experimental evidence for the tandem electrocatalysis mechanism without iR correction. a-c) LSV curves before and after passivating at 0.4 V (versus RHE) for 10 min of a) Pt/C, b) Ru/C, and c) Pt1-Ru/C. d-f) LSV curves before and after immersing in DMSO aqueous solution for 1 min of d) Pt/C, e) Ru/C, and f) Pt1-Ru/C. Source data are provided as a Source Data file.

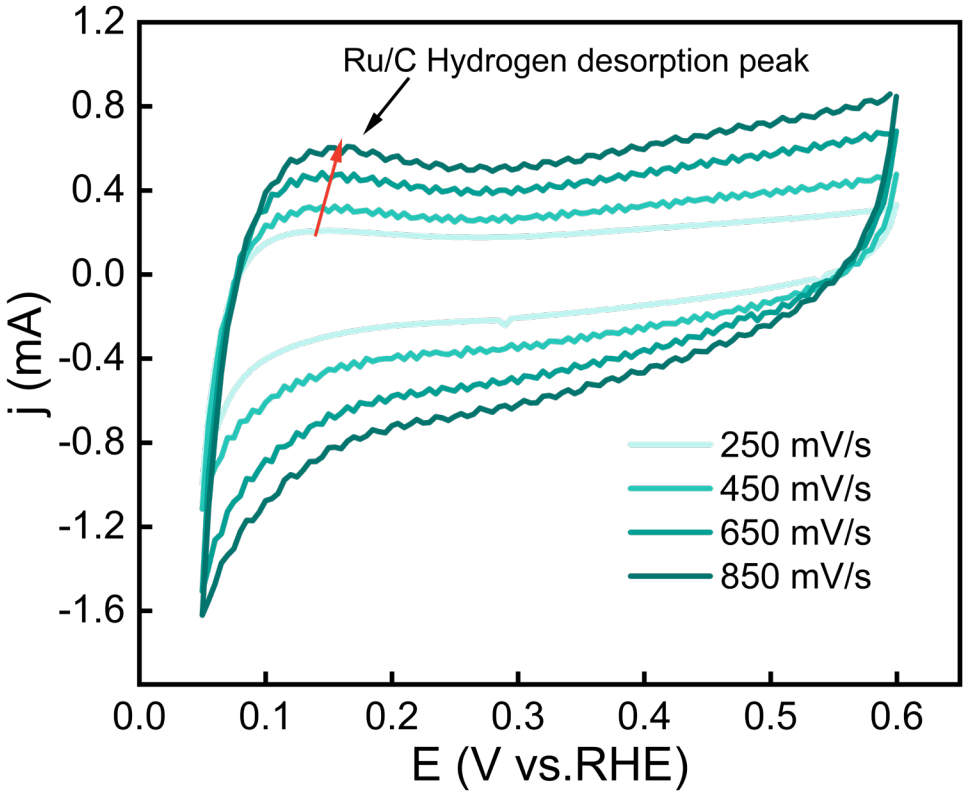

Supplementary Fig. 36: The CV curves of Ru/C catalyst with different scan rate in a N_2-saturated 0.5 M H_2SO_4. These CV data were iR correction free. Source data are provided as a Source Data file.

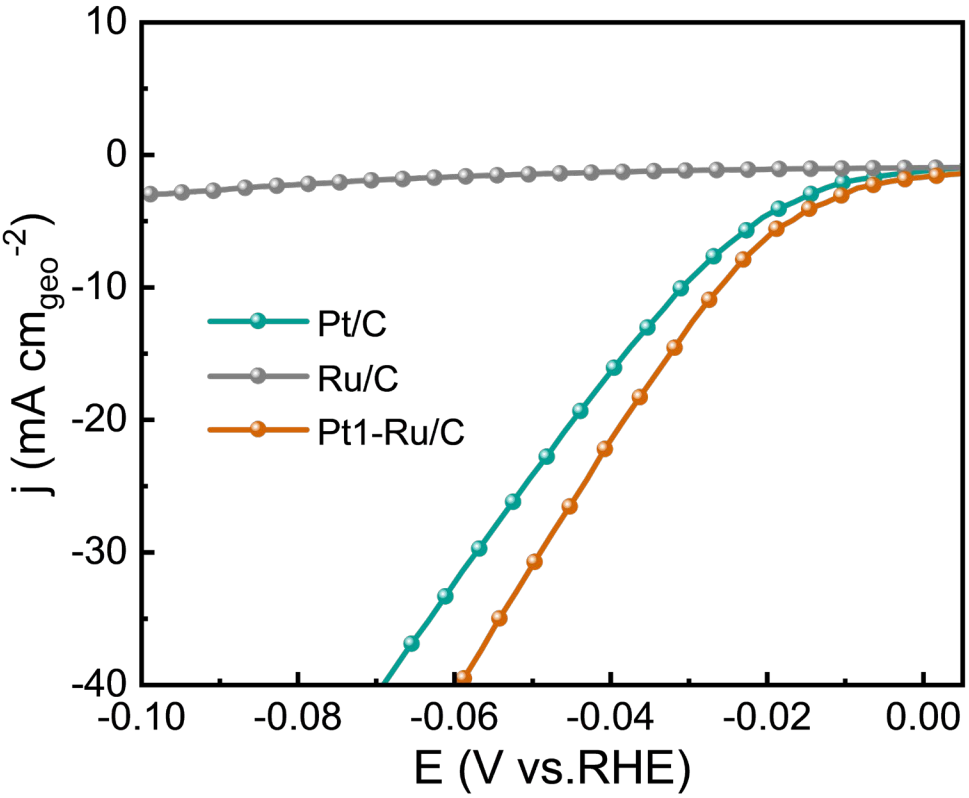

Supplementary Fig. 37: HER polarization curves of different catalysts in N_2-saturated 0.5 M H_2SO_4 with a rotating speed of 1,600 rpm without iR correction. Source data are provided as a Source Data file.

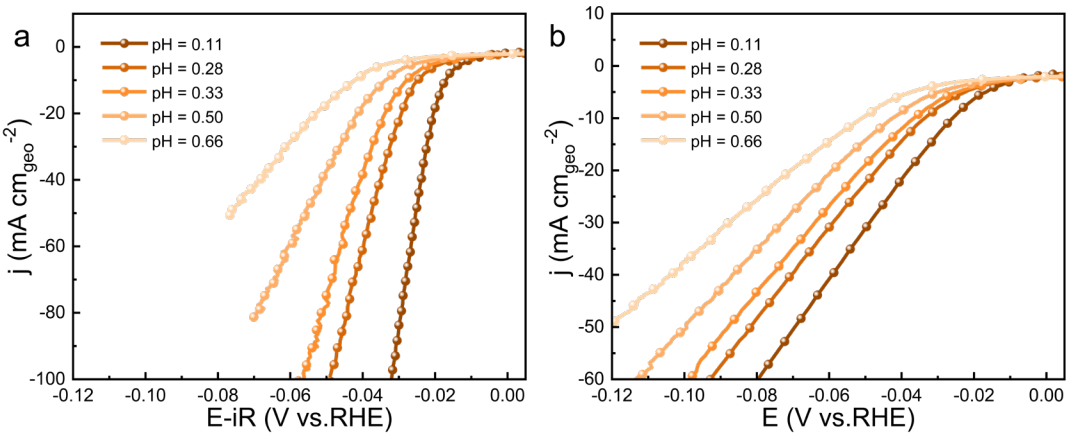

Supplementary Fig. 38: a) The HER polarization curves of Pt1-Ru/C in different pH. Different pH H_2SO_4 solutions were prepared by adding varying volumes of water to the 0.5 M H_2SO_4 solution. The pH value measured in 0.5 M H_2SO_4 solution is 0.11±0.03. b) The HER polarization curves of Pt1-Ru/C in different pH without iR correction. Source data are provided as a Source Data file.

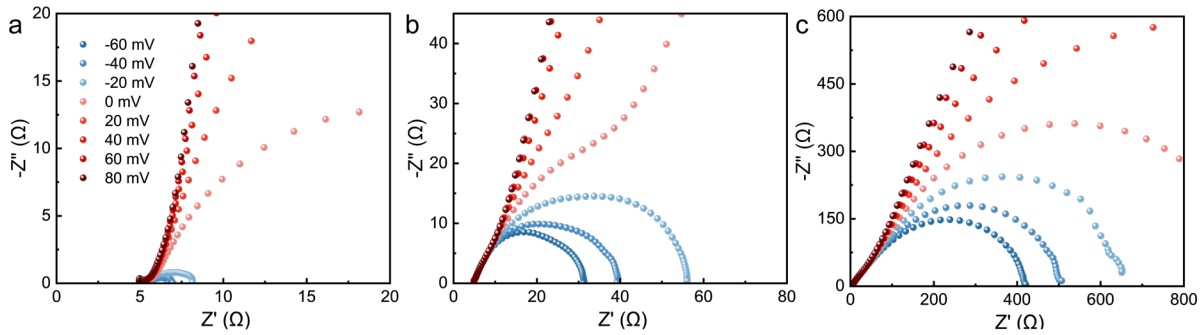

Supplementary Fig. 39: In situ EIS plots on a) Pt1-Ru/C, b) Pt/C, c) Ru/C. The EIS was measured at different overpotentials in a H_2-saturated 0.5 M H_2SO_4 solution with an amplitude voltage of 5 mV in a frequency range of 100 kHz-0.1 KHz. Source data are provided as a Source Data file.

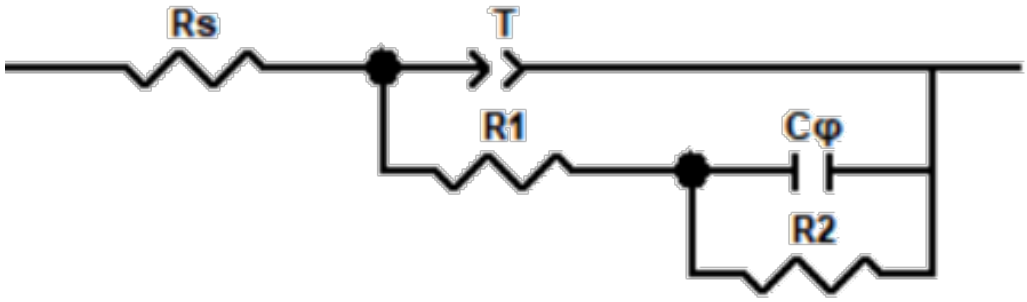

Supplementary Fig. 40: The equivalent circuit for the EIS simulation. Rs represents the solution resistance. T and R_1 represent the double layer capacitance and the catalytic charge transfer resistance, respectively. C_φ and R_2 are the hydrogen diffusion and adsorption pseudo-capacitance and resistance, respectively.[4]

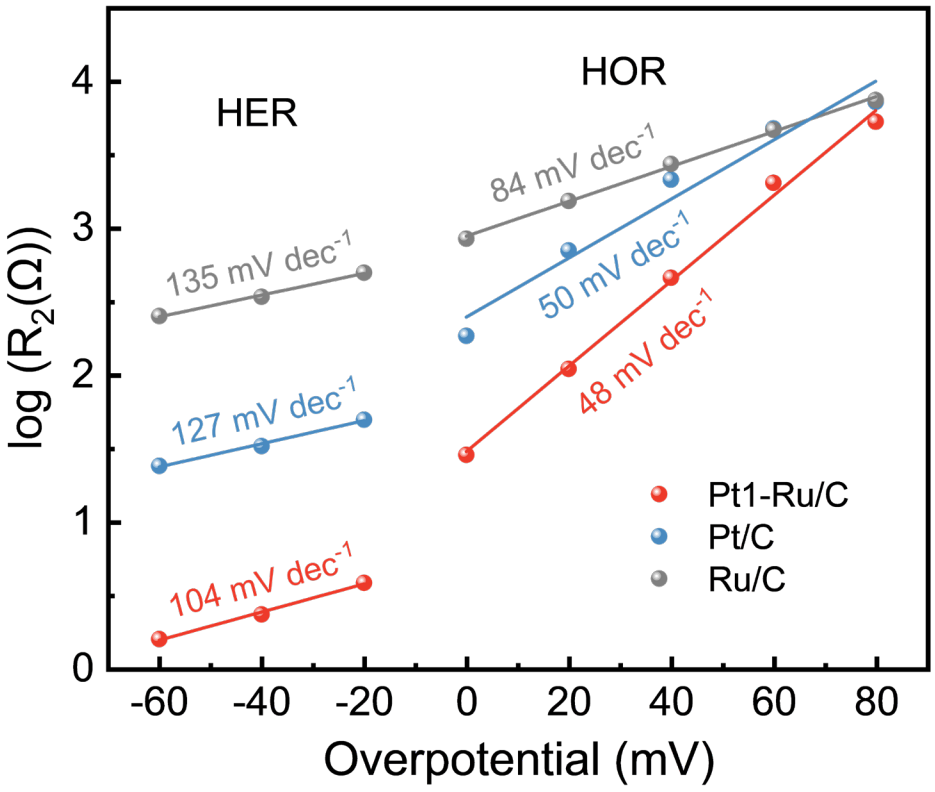

Supplementary Fig. 41: EIS-derived Tafel plots of different catalysts. Source data are provided as a Source Data file.

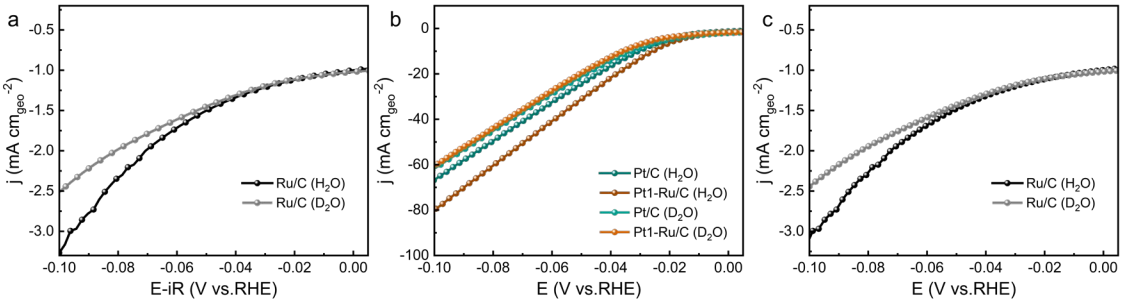

Supplementary Fig. 42: a) HER polarization curves of Ru/C catalyst in N_2-saturated 0.5 M H_2SO_4 aqueous solution and N_2-saturated 0.5 M D_2SO_4 heavy water (D_2O) solution. All LSV data were carried out at a scan rate of 0.5 mV s^{-1} with 90% iR compensation on a RDE at 1600 rpm. The ohmic resistance ($5 \pm 0.3\,\Omega$) for iR compensation was obtained from EIS analysis with a geometric area of 0.19625 cm^2. b) HER polarization curves of Pt/C and Pt1-Ru/C catalysts in N_2-saturated 0.5 M H_2SO_4 aqueous solution and N_2-saturated 0.5 M D_2SO_4 deuterium oxide (D_2O) solution without iR correction. c) HER polarization curves of Ru/C and Pt1-Ru/C catalysts in N_2-saturated 0.5 M H_2SO_4 aqueous solution and N_2-saturated 0.5 M D_2SO_4 deuterium oxide (D_2O) solution without iR correction. Source data are provided as a Source Data file.

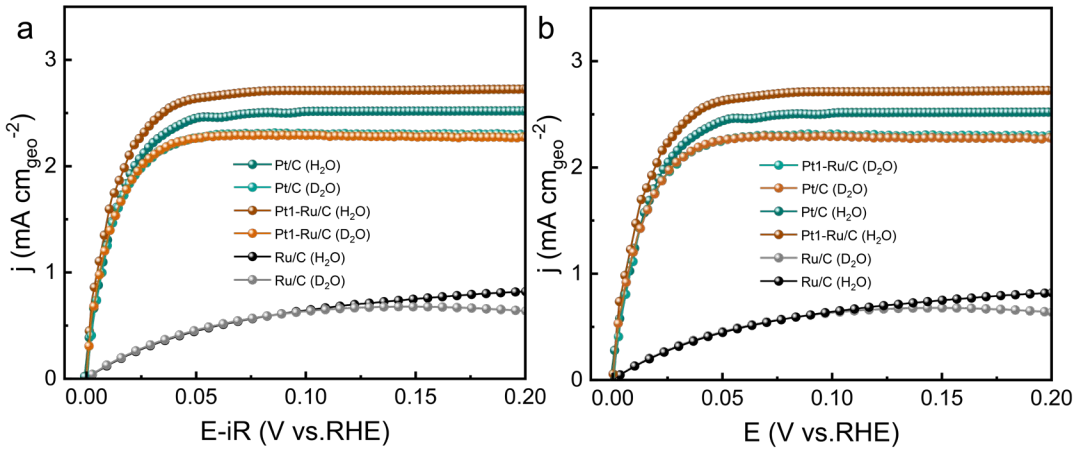

Supplementary Fig. 43: a) HOR polarization curves of Pt/C, Pt1-Ru/C, and Ru/C catalysts in H_2-saturated 0.5 M H_2SO_4 aqueous solution and H_2-saturated 0.5 M D_2SO_4 heavy water (D_2O) solution. All LSV data were carried out at a scan rate of 0.5 mV s^{-1} with 90% iR compensation on a RDE at 1600 rpm. The ohmic resistance ($5 \pm 0.3\ \Omega$) for iR compensation was obtained from EIS analysis with a geometric area of 0.19625 cm^2. b) HOR polarization curves of Pt/C, Pt1-Ru/C, and Ru/C catalysts in H_2-saturated 0.5 M H_2SO_4 aqueous solution and H_2-saturated 0.5 M D_2SO_4 heavy water (D_2O) solution without iR correction. Source data are provided as a Source Data file.

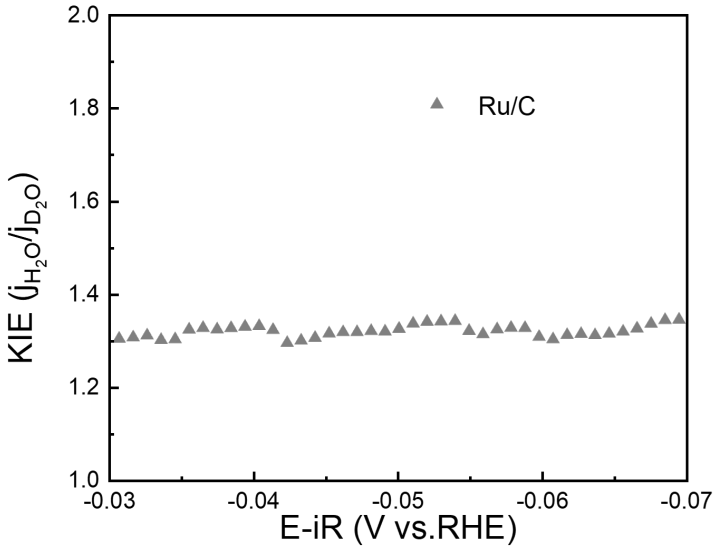

Supplementary Fig. 44: H/D isotope effect analysis (j_{H_2O}/j_{D_2O} *vs.* potential) for Pt/C and Pt1-Ru/C in -0.03 V - -0.07 V (*vs.* RHE). Source data are provided as a Source Data file.

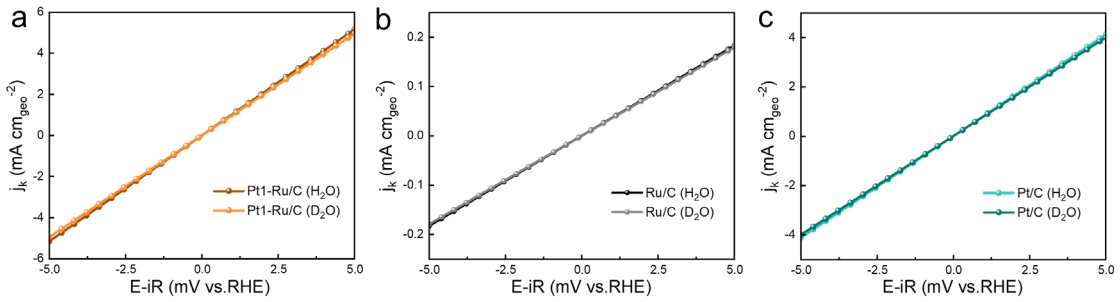

Supplementary Fig. 45: Linear region of kinetic current density (j_k) (calculated based on the Koutecky-Levich equation) of a) Pt1-Ru/C, b) Ru/C, and c) Pt/C. All LSV data were carried out at a scan rate of 0.5 mV s^{-1} with 90% iR compensation on a RDE at 1600 rpm. The ohmic resistance ($5 \pm 0.3\ \Omega$) for iR compensation was obtained from EIS analysis with a geometric area of 0.19625 cm^2. Source data are provided as a Source Data file.

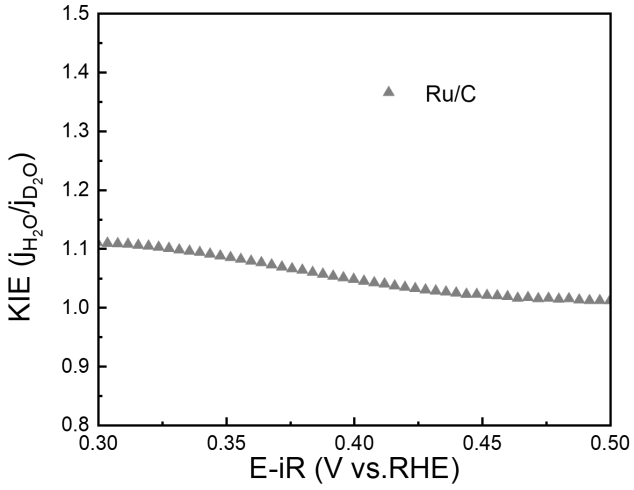

Supplementary Fig. 46: H/D isotope effect analysis (j_{H_2O}/j_{D_2O} *vs.* potential) for Pt/C and Pt1-Ru/C in 0.30 V - 0.50 V (*vs.* RHE). Source data are provided as a Source Data file.

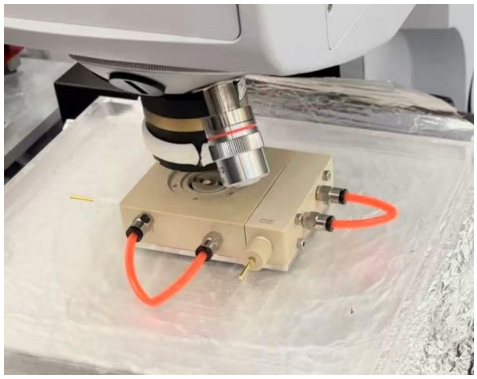

Supplementary Fig. 47: The digital picture of in situ synchrotron FTIR setup.

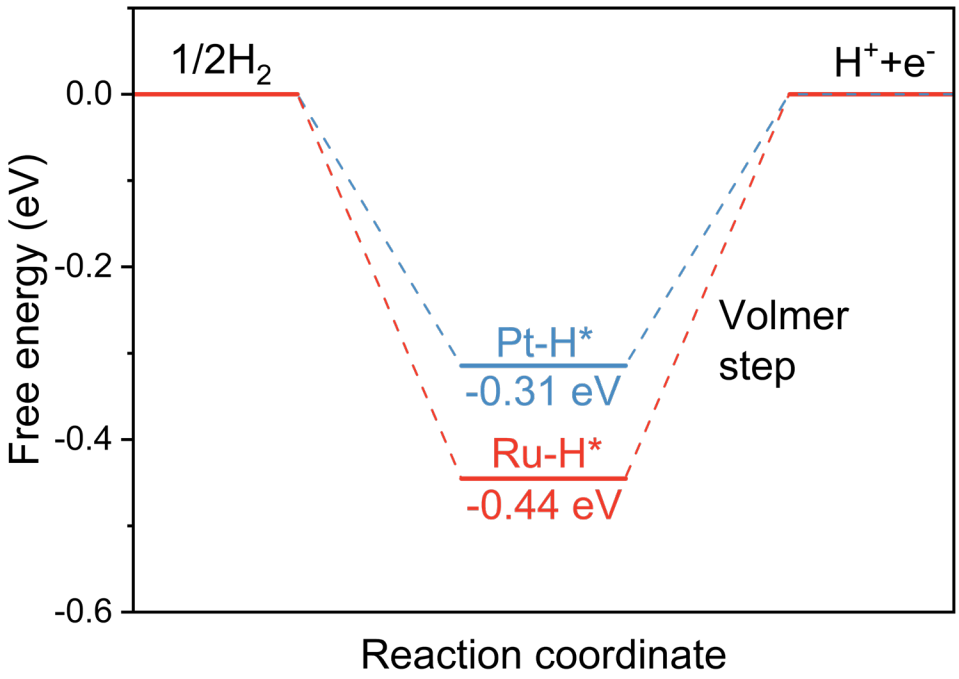

Supplementary Fig. 48: Gibbs free energy diagram for HOR on pure Pt and pure Ru. Source data are provided as a Source Data file.

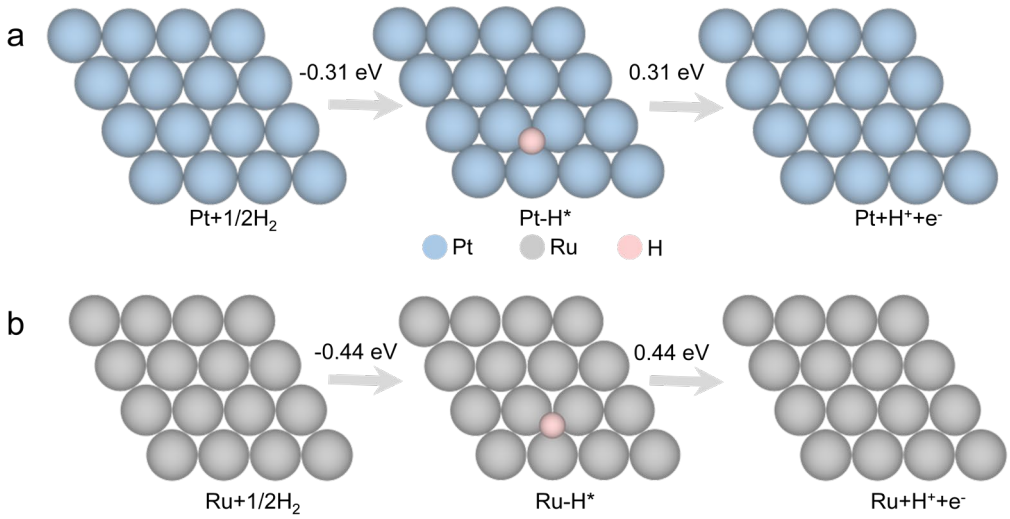

Supplementary Fig. 49: a) Pure Pt and b) pure Ru models and schematic diagrams of the H* transfer process as well as the corresponding free energy in each step. Source data are provided as a Source Data file.

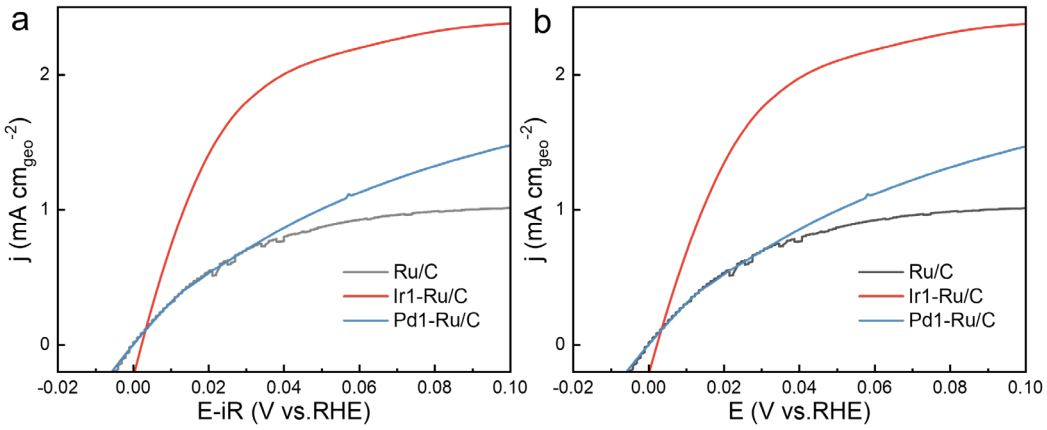

Supplementary Fig. 50: a) HOR polarization curves of Ru/C, Ir1-Ru/C, and Pd1-Ru/C catalysts in H_2-saturated 0.5 M H_2SO_4 aqueous solution. All LSV data were carried out at a scan rate of 0.5 mV s^{-1} with 90% iR compensation on a RDE at 1600 rpm. The ohmic resistance ($5 \pm 0.3\ \Omega$) for iR compensation was obtained from EIS analysis with a geometric area of 0.19625 cm^2. b) HOR polarization curves of Ru/C, Ir1-Ru/C, and Pd1-Ru/C catalysts in H_2-saturated 0.5 M H_2SO_4 aqueous solution without iR correction. Source data are provided as a Source Data file.

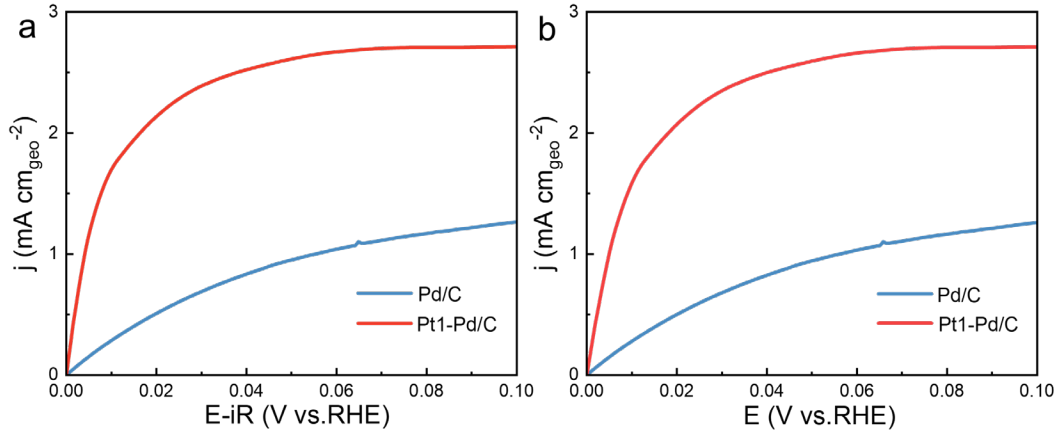

Supplementary Fig. 51: HOR polarization curves of Pd/C and Pt1-Pd/C catalysts in H_2-saturated 0.5 M H_2SO_4 aqueous solution. All LSV data were carried out at a scan rate of 0.5 mV s^{-1} with 90% iR compensation on a RDE at 1600 rpm. The ohmic resistance ($5 \pm 0.3\ \Omega$) for iR compensation was obtained from EIS analysis with a geometric area of 0.19625 cm^2. b) HOR polarization curves of Pd/C and Pt1-Pd/C catalysts in H_2-saturated 0.5 M H_2SO_4 aqueous solution without iR correction. Source data are provided as a Source Data file.

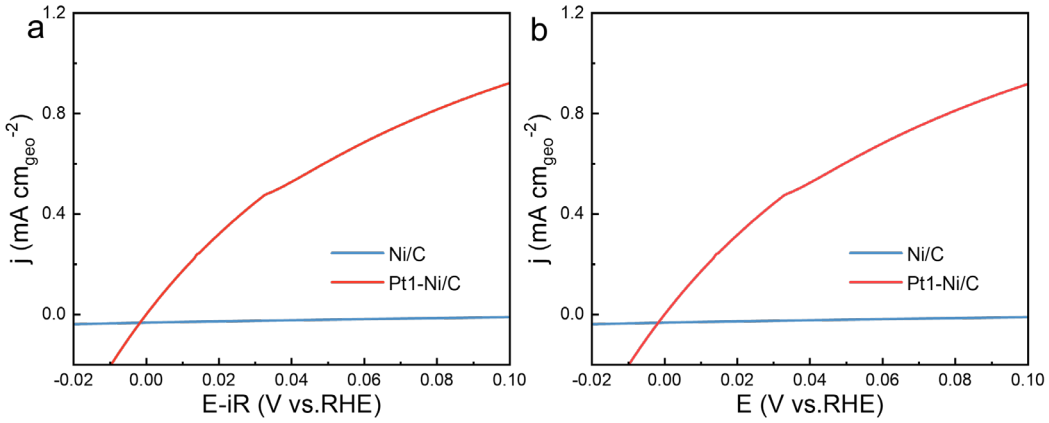

Supplementary Fig. 52: a) HOR polarization curves of Ni/C and Pt1-Ni/C catalysts in H_2-saturated 0.5 M H_2SO_4 aqueous solution. All LSV data were carried out at a scan rate of 0.5 mV s^{-1} with 90% iR compensation on a RDE at 1600 rpm. The ohmic resistance ($5 \pm 0.3\ \Omega$) for iR compensation was obtained from EIS analysis with a geometric area of 0.19625 cm^2. b) HOR polarization curves of Ni/C and Pt1-Ni/C catalysts in H_2-saturated 0.5 M H_2SO_4 aqueous solution without iR correction. Source data are provided as a Source Data file.

Supplementary Tables

Supplementary Table 1. Mass percent of Ru and Pt in different samples determined by ICP.

mass percent	Ru	Pt
Ru/C	1.076%	0%
Pt1-Ru/C-0.5	1.123%	0.079%
Pt1-Ru/C	1.105%	0.145%
Pt1-Ru/C-2	1.224%	0.226%
Pt1/C	0%	0.102%

Supplementary Table 2. EXAFS fitting parameters at the Ru K-edge for samples.

		Ru K-edge				
Sample	**Shell**	***N***	***R* (Å)**	**σ^2 (Å^2)**	**ΔE_0 (eV)**	***R* factor**
Ru foil	Ru-Ru	12.0	2.68±0.03	0.0018±0.0005	-3.2	0.0010
Ru/C	Ru-Ru	5.6±0.2	2.68±0.04	0.0023±0.0004	-5.8	0.0009
Pt1-Ru/C-0.5	Ru-Ru	5.8±0.3	2.68±0.02	0.0017±0.0002	-5.2	0.0008
Pt1-Ru/C	Ru-Ru	5.9±0.3	2.69±0.01	0.0016±0.0005	-3.8	0.0011
Pt1-Ru/C-2	Ru-Ru	5.9±0.4	2.68±0.05	0.0007±0.0006	-9.0	0.0046
Pt1-Ru/C-0.5-A	Ru-Ru	5.4±0.1	2.68±0.04	0.0010±0.0002	-8.7	0.0032
Pt1-Ru/C-A	Ru-Ru	5.7±0.2	2.68±0.06	0.0021±0.0004	-9.6	0.0038
Pt1-Ru/C-2-A	Ru-Ru	5.7±0.3	2.69±0.05	0.0008±0.0003	-3.6	0.0011

Supplementary Table 3. EXAFS fitting parameters at the Pt L_3-edge for samples.

Sample	Shell	Pt L_3-edge N	R(Å)	σ^2(Å^2)	ΔE_0(eV)	R factor
PtO_2	Pt-O	6.0	2.01±0.03	0.0030±0.0005	6.6	0.0018
H_2PtCl_6	Pt-Cl	6.0	2.32±0.04	0.0027±0.0007	8.1	0.0033
Pt1/C	Pt-Cl	3.6±0.2	2.30±0.02	0.0046±0.0011	6.9	0.0023
Pt1-Ru/C-0.5	Pt-Cl	3.2±0.1	2.29±0.03	0.0047±0.0014	7.0	0.0025
Pt1-Ru/C	Pt-Cl	3.4±0.3	2.29±0.06	0.0048±0.0020	6.5	0.0011
Pt1-Ru/C-2	Pt-Cl	3.5±0.3	2.28±0.05	0.0050±0.0021	6.0	0.0028
Pt1-Ru/C-0.5-A	Pt-O	1.5±0.2	2.04±0.03	0.0011±0.0005	9.1	0.0015
	Pt-Cl	0.5±0.1	2.31±0.01	0.0013±0.0008		
Pt1-Ru/C-A	Pt-O	1.4±0.3	2.08±0.02	0.0030±0.0009	4.7	0.0038
	Pt-Cl	0.5±0.1	2.28±0.04	0.0035±0.0010		
	Pt-Ru	0.7±0.2	2.68±0.04	0.0075±0.0024		
Pt1-Ru/C-2-A	Pt-O	1.2±0.4	2.00±0.06	0.0030±0.0011	6.8	0.0022
	Pt-Cl	0.8±0.2	2.31±0.05	0.0026±0.0015		
	Pt-Ru	0.4±0.1	2.70±0.03	0.0084±0.0033		

Note: S_0^2 were set to 0.831 and 0.923 for Pt and Ru, respectively, according to the experimental EXAFS fit of Pt-foil and Ru-foil by fixing N as the known crystallographic value.

N - coordination numbers;

R - bond distance (the bond length between central atoms and surrounding coordination atoms);

σ^2 - Debye-Waller factors (a measure of thermal and static disorder in absorber-scatterer distances);

ΔE_0 - the inner potential correction;

R factor – the goodness of fit.

Error bounds that characterize the structural parameters obtained by EXAFS spectroscopy were estimated as N ± 20%; R ± 1%; σ^2 ± 20%; ΔE_0 ± 20%. For comparison, the interatomic distances and coordination numbers for the references (Ru-foil, H_2PtCl_6, and PtO_2) were calculated from their crystallographic structures.

Supplementary Table 4. Ratio of Pt^{2+} before and after HOR test in different samples.

$Pt^{2+}/(Pt^{2+}+Pt^{4+})$	**before HOR testing**	**0.1 V-3 h**
Pt1-Ru/C-0.5	49.7%	71.9%
Pt1-Ru/C	46.1%	69.9%
Pt1-Ru/C-2	42.2%	62.4%

Supplementary Table 5. Performance comparison of the PEMFCs reported in literatures.[5-22]

Anode (loading$_{PGM}$)	PPD (W/cm^2)	Anode mass activity @0.6 V (A mg$_{PGM}^{-1}$)	Stability	Ref.
Pt1-Ru/C (0.005 mg cm-^{2})	1.91 (O_2) 0.95 (Air)	520 260	20% current loss @0.6 V, 40 h (Air)	This work
Ir_1-P_1/NPG (0.0045 mg cm-^{2})	1.93 (O_2) 1.06 (Air)	511 333	30 mV voltage loss @1.0 A cm^{-2}, 35 h (O_2)	5
Pt@WN/rGO (0.05 mg cm^{-2})	1.442 (O_2) 0.826 (Air)	40 22	4.6% current loss @0.6 V, 50 h (O_2)	6
IrRh@C_{ZIF-8} (0.024 mg cm^{-2})	1.361 (O_2) -	62.5 -	-	7
Pd/C (1 mg cm^{-2})	0.64 (O_2) -	0.65 -	A constant current density @0.2 A cm^{-2}, 100 h (O_2)	8
$PtMo_1$/KB (0.02 mg cm^{-2})	0.85 (O_2) -	72.27 -	-	9
PtW_6O_{24}-CDs-4 (0.01 mg cm^{-2})	0.14 (O_2) -	20 -	0.8 V to 0.7 V @10 mA cm^{-2}, 12 h (O_2)	10
Ir_{NP}@Ir_{SA}-N-C (0.024 mg cm^{-2})	1.20 (O_2) -	58.01 -	-	11
Pt-Ni_{SA}/CNT-2.6 (0.05 mg cm^{-2})	1.65 (O_2) -	48 -	-	12
PtRu@RuO_2/C (0.4 mg cm^{-2})	1.65 (O_2) -	4.375 -	-	13
Pt/C-PANI-5 (0.2 mg cm^{-2})	1.49 (O_2) -	9 -	-	14
Pt/C:DhmPy=2:1 (0.5 mg cm^{-2})	1.69 (O_2) -	2.8 -	-	15
Pt/C MFP90° (1 mg cm^{-2})	0.22 (O_2) -	0.3 -	-	16
PtSn/VC (3)	-	-	85% of PPD was	17

(0.16 mg cm^{-2})	0.01 (Air)	0.8125	retained after 60 000 cycles (Air)	
Cu/Pt (0.5) (0.624 mg cm^{-2})	- 0.005 (Air)	- 0.096	A stable voltage @90 mA cm^{-2}, 5 h (Air)	18
IrRu4/22 KB (0.053 mg cm^{-2})	1.46 (O_2) -	43.4 -	-	19
Pt-Er/h-NC (0.05 mg cm^{-2})	0.74 (O_2) -	30 -	-	20
Pt@MCL (0.05mg cm^{-2})	0.687 (O_2) -	12 -	-	21
CNTs@VO_2−Pt (0.35 mg cm^{-2})	0.831 (O_2) -	2.3 -	A relatively constant voltage @0.9 V, 200 h (O_2)	22

Supplementary Table 6. The noble metal constituent components of the catalyst, the cost of the anode catalyst, and the peak of anode cost-specific power.

Catalyst	Components	Anode cost ($/cm^2)	anode cost/P_{max} ($/KW)
Pt1-Ru/C	1.105 wt% Ru, 0.145 wt% Pt	7.86E-05	1.8
Pt/C	30 wt% Pt	1.73E-03	41.1

Note: The price of Ru metal is $13.25/g, and the price of Pt metal is $34.51/g (as of May 27, 2024). When calculating the cost of the anode catalyst, the price of the carbon support is ignored.

Supplementary Table 7. EIS fitting results of different samples.

Catalyst	η (mV)	R_s (Ω)	T (F S^{n-1})	R_1 (Ω)	R_2 (Ω)	C_φ (F)
Pt1-Ru/C	80	5.22±0.12	0.002106	4.3±0.2	5325±125	0.001162
	60	4.93±0.24	0.001818	2.2±0.1	2041±103	0.001528
	40	5.13±0.25	0.002198	2.1±0.1	460.3±56	0.001708
	20	5.10±0.37	0.002684	1.8±0.3	110.1±23	0.002335
	0	5.03±0.35	0.000454	1.6±0.4	28.6±6.2	0.004536
	-20	5.00±0.17	0.000215	1.0±0.5	3.8±0.8	0.004593
	-40	4.93±0.54	0.000472	0.6±0.3	2.3±0.5	0.005632
	-60	4.86±0.42	0.000543	0.7±0.2	1.6±0.2	0.005862
Pt/C	80	4.99±0.51	0.000242	35.3±0.5	7259±226	0.000060
	60	5.00±0.21	0.000247	36.9±0.4	4779±146	0.000059
	40	5.02±0.32	0.000273	46.3±0.4	2142±82	0.000063
	20	5.02±0.43	0.000356	79.7±0.7	706.3±34	0.000107
	0	4.88±0.37	0.000475	72.0±0.6	184.9±23	0.000472
	-20	4.68±0.70	0.000672	3.9±0.2	49.6±15	0.000006
	-40	4.64±0.41	0.000572	2.8±0.1	32.8±11	0.000009
	-60	4.70±0.52	0.000354	3.0±0.4	24±3.2	0.000010
Ru/C	80	4.55±0.52	0.000150	281.8±0.3	7483±345	0.000020
	60	4.53±0.31	0.000150	277.5±0.2	4691±256	0.000019
	40	4.51±0.42	0.000149	270.6±0.1	2745±228	0.000019
	20	4.52±0.21	0.000145	258.0±0.3	1534±156	0.000019
	0	4.55±0.11	0.000135	234.6±0.4	849.7±78	0.000021
	-20	4.69±0.64	0.000103	179.4±0.4	497.8±56	0.000025
	-40	4.71±0.53	0.000099	173.7±0.5	340.7±24	0.000025
	-60	4.73±0.47	0.000089	173.1±0.6	252.1±23	0.000024

References

1 Zhuang, Z. *et al.* Nickel supported on nitrogen-doped carbon nanotubes as hydrogen oxidation reaction catalyst in alkaline electrolyte. *Nat. Commun.* **7**, 10141 (2016).

2 Zhang, B. *et al.* Lattice-Confined Ir Clusters on Pd Nanosheets with Charge Redistribution for the Hydrogen Oxidation Reaction under Alkaline Conditions. *Adv. Mater.* **33**, 2105400 (2021).

3 Song, F. *et al.* Interfacing nickel nitride and nickel boosts both electrocatalytic hydrogen evolution and oxidation reactions. *Nat. Commun.* **9**, 4531 (2018).

4 Lazanas, A. C. & Prodromidis, M. I. Electrochemical Impedance Spectroscopy—A Tutorial. *ACS Meas. Sci. Au.* **3**, 162-193 (2023).

5 Wang, Q. *et al.* Atomic metal–non-metal catalytic pair drives efficient hydrogen oxidation catalysis in fuel cells. *Nat. Catal.* **6**, 916-926 (2023).

6 Cai, B. *et al.* Unlocking Superior Hydrogen Oxidation and CO Poisoning Resistance on Pt Enabled by Tungsten Nitride-Mediated Electronic Modulation. *J. Am. Chem. Soc.* **146**, 33193-33203 (2024).

7 Wang, X. *et al.* Single atom sites as CO scavenger to allow for crude hydrogen usage in PEMFC. *Sci. Bull.* **69**, 1061-1070 (2024).

8 Huang, G. *et al.* Lattice Hydrogen Boosts CO Tolerance of Pd Anode Catalysts in High-Temperature Proton Exchange Membrane Fuel Cells. *Adv. Funct. Mater.* **35**, 2415358 (2025).

9 Jin, C. *et al.* Low-Pt anodes with gradient molybdenum isomorphism for high performance and anti-CO poisoning PEMFCs. *Nano Energy* **122**, 109305 (2024).

10 Zhou, Y. *et al.* Carbon dots/PtW_6O_{24} composite as efficient and stable electrocatalyst for hydrogen oxidation reaction in PEMFCs. *Chem. Eng. J.* **426**, 130709 (2021).

11 Yang, X. *et al.* CO-Tolerant PEMFC Anodes Enabled by Synergistic Catalysis between Iridium Single-Atom Sites and Nanoparticles. *Angew. Chem. Int. Ed.* **60**, 26177-26183 (2021).

12 Lin, J. *et al.* Synergy between single atom and nanoclusters promotes power and CO tolerant performance in PEMFCs. *Chem. Eng. J.* **506**, 160156 (2025).

13 Chen, L. *et al.* Enhancing CO Tolerance in PEMFC Anodes via Thermal Oxidation Induced RuO_2 Blocking Shell on a PtRu/C Catalyst. *Nano Lett.* **24**, 10642-10649 (2024).

14 Shi, X., Song, W., Wei, T., Zhang, K. & Shao, Z. Improved CO tolerance of Pt nanoparticles on polyaniline-modified carbon for PEMFC anode. *Fuel* **382**, 133239 (2025).

15 Zhang, D., Liu, W., Ye, K. & Li, X. High CO and sulfur tolerant proton exchange membrane fuel cell anodes enabled by "work along both lines" mechanism of 2,6-dihydroxymethyl pyridine molecule blocking layer. *J. Colloid Interface Sci.* **653**, 413-422 (2024).

16 Ramos, A. S. *et al.* High CO tolerance of Pt nanoparticles synthesized by sodium borohydride in a time-domain NMR spectrometer. *Int. J. Hydrogen Energy* **45**, 22973-22978 (2020).

17 Sapkota, P., Lim, S. & Aguey-Zinsou, K.-F. Platinum–tin as a superior catalyst for proton exchange membrane fuel cells. *RSC Sustainability* **1**, 368-377 (2023).

18 Sapkota, P., Boyer, C., Lim, S. & Aguey-Zinsou, K.-F. High performing platinum—copper catalyst for self—breathing polymer electrolyte membrane fuel cell. *Res. Chem. Intermed.* **48**, 3019-3037 (2022).

19 You, E., Lee, S. W., You, D., Lee, B. & Pak, C. Effect of Metal Composition and Carbon Support on the Durability of the Reversal-Tolerant Anode with IrRu Alloy Catalyst. *Catalysts* **10**, 932 (2020).

20 Chen, G. *et al.* Near-Atomic-Scale Superfine Alloy Clusters for Ultrastable Acidic Hydrogen Electrocatalysis. *J. Am. Chem. Soc.* **145**, 22069-22078 (2023).

21 Ko, K. *et al.* Redesign of Anode Catalyst for Sustainable Survival of Fuel Cells. *Adv. Sci.* **11**, 2307073 (2024).

22 Lin, L. *et al.* H Induced Metal-Insulation Transition Boosts the Stability of High Temperature Polymer Electrolyte Membrane Fuel Cells. *Angew. Chem. Int. Ed.* **64**, e202419919 (2025).